Geochemistry 83 (2023) 125949

Contents lists available at ScienceDirect

Geochemistry

journal homepage: www.elsevier.com/locate/chemer

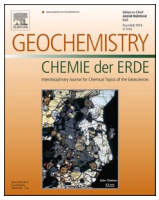

Fluid source and physicochemical conditions of the polymetallic mineralization in Gawuch Formation, Kohistan Island Arc, NW Pakistan

Muhammad Farhan [a], Mohammad Arif [b,c], Ying Ye [a], Chun-Feng Li [a,d,e,*], Xuegang Chen [a,d], Dieter Garbe-Schönberg [f], Tao Wu [a,d], Zaheen Ullah [g,k], Zahid Hussain [a], Tehseen Zafar [h,l,**], Izhar Sadiq [a], Syed Wajid Hanif Bukhari [i], Asad Khan [j]

[a] Department of Marine Sciences, Zhejiang University, Zhoushan 316021, China
[b] Department of Earth Sciences, Abbottabad University of Science and Technology, Havelian 22500, Pakistan
[c] Department of Geology, University of Peshawar, Peshawar 25120, Pakistan
[d] Hainan Institute, Zhejiang University, Sanya 572025, China
[e] Laboratory of Marine Mineral Resources, Qingdao National Laboratory for Marine Science and Technology, Qingdao 266237, China
[f] CAU Kiel University, Institute of Geosciences, D-24118 Kiel, Germany
[g] Department of Geology, University of Baltistan Skardu, 16100, Pakistan
[h] State Key Laboratory of Ore Deposit Geochemistry, Institute of Geochemistry, Chinese Academy of Sciences, Guiyang 550081, China
[i] Centre of Excellence in Mineralogy, University of Balochistan, Quetta 87300, Pakistan
[j] Department of Geology, FATA University, FR Kohat 26100, KP, Pakistan
[k] Key Laboratory of Metallogenic Prediction of Nonferrous Metals and Geological Environment Monitoring, Ministry of Education, School of Geosciences and Info-Physics, Central South University, Changsha 410083, China
[l] School of Earth and Space Sciences, Peking University, Beijing, China

ARTICLE INFO

Handling Editor: Astrid Holzheid

Keywords:
Fluid source
Sulfides geochemistry
Physicochemical conditions
S-isotope
Kohistan arc

ABSTRACT

The Cu-Sb-Pb polymetallic vein deposit is hosted by metavolcanics rocks of the Gawuch Formation at the Kaldom Gol area of the northwest Kohistan arc terrain in northern Pakistan. The mineralization is closely associated with the dioritic to granodioritic rocks of the Lowari pluton, which was intruded into the Gawuch metavolcanics. Details of ore characterization and processes of ore genesis of this evidently hydrothermal mineralization are not well documented. Integrating petrographic, mineral-chemical and isotopic investigations, this study aims to comprehend the source of hydrothermal fluids, geochemical evolution, mineral inclusions and physicochemical conditions of the Cu-Sb-Pb polymetallic vein deposit in Gawuch metavolcanics in the Kohistan arc terrain in northern Pakistan. The mineralization is distinguished into three types of ore-gangue associations: Type Ia, Type Ib, and Type II. The textural study revealed two pyrite generations: (i) Py1 displaying euhedral to subhedral habits and containing scarce inclusions, and (ii) Py2 occurring as anhedral grains hosting abundant inclusions. Type Ia is characterized by Py1 associated with abundant quartz (Qz) showing comb texture, sericite (Ser), and minor chlorite (Chl). Type Ib comprises Qz + Ser + Chl and Py2, chalcopyrite (Ccp), and magnetite (Mag). Type II is represented by mosaic quartz, rhombic adularia, and bladed calcite, and the ore minerals fahlore and galena. Alteration zones composed of Qz-Ser ± Chl and Qz-Ser-Chl, surround Type I (a, b) and Type II veins, respectively. Fahlore and galena mostly replace pyrite of Type Ia and chalcopyrite of Type Ib. In addition, malachite, azurite, hematite and covellite occur as secondary (supergene) minerals. The Co/Ni ratios (>1) of Kaldom Gol pyrites suggest that the ore-forming fluids were hydrothermal in origin and Py1 and Py2 solidified at 221–304 °C and 225–261 °C, respectively. The LA-ICP-MS time-resolved depth profiles confirm the existence of sphalerite, and chalcopyrite inclusions in pyrite (Py1 and Py2) and *millerite*, *bravoite*, *vaesite*, Au-tellurides, native Au and galena inclusions in chalcopyrite and fahlore. Sulfur isotope compositions of pyrites ($\delta^{34}S$ = Py1, −0.58 to +2 ‰; $\delta^{34}S$ = Py2, −0.24 to +2.04 ‰) indicate that the ore-forming fluids were derived from magmatic source (s). The mineral assemblage, hydrothermal alterations, textures, temperature and $\delta^{34}S$ of pyrites suggest that the Cu-Sb-Pb polymetallic mineralization at Kaldom Gol represents an intermediate-sulfidation type of epithermal deposit.

* Correspondence to: C.-F. Li, Department of Marine Sciences, Zhejiang University, Zhoushan 316021, China.
** Corresponding author.
E-mail addresses: cfli@zju.edu.cn (C.-F. Li), zafar@vip.gyig.ac.cn (T. Zafar).

https://doi.org/10.1016/j.chemer.2022.125949
Received 30 June 2022; Received in revised form 25 December 2022; Accepted 28 December 2022
Available online 4 January 2023

1. Introduction

Major magmatic-hydrothermal deposits, such as porphyry Cu–Mo–Au, epithermal Au-Ag, volcanic-hosted massive sulfide (VMS) and podiform chromite deposits are closely associated with island arcs (Mitchell and Bell, 1973; Herrington and Brown, 2011). Northern Pakistan, which comprises various geological settings and a complex history of crustal evolution associated with Neo-Tethys (intra-oceanic) subduction that formed Kohistan Island Arc, presents one of the most favorable locales for mineral deposit formation (Fig. 1A). In fact, the northern regions of Pakistan contain several economic mineral deposits, including placer deposits (Bagrote valley), gemstone (Shigar Valley), porphyry-style Cu (Au, Mo) and breccia related epithermal gold (Cu, Ag) deposits (Drosh-Shishi areas) and sulfide-bearing hydrothermal quartz veins (e.g., Drosh, Astore and Machallu areas) (Agheem et al., 2011; Tahirkheli et al., 2012; Anjum et al., 2018; Alam et al., 2019; Ali et al., 2021; Farhan et al., 2021a; Farhan et al., 2021b; Hussain et al., 2021).

The Kaldom Gol area in the north-western part of Kohistan Island Arc, Pakistan (Fig. 1A, B) is well-known for hosting polymetallic (Cu-Sb-Pb) quartz vein mineralization in the metavolcanics rocks of the Gawuch Formation (Tahirkheli et al., 2005; Tahirkheli et al., 2012; Farhan et al., 2021b). The Cretaceous Gawuch Formation comprises variably metamorphosed sedimentary (quartzite and marble) and basalt to andesitic volcanic rocks that host Eocene (~42 Ma) polymetallic quartz veins (Tahirkheli et al., 2012; Zaman and Bamousa, 2015). The primary minerals in metavolcanic rocks are plagioclase, amphibole and quartz; secondary minerals include chlorite, epidote, and trace amounts of clay (illite/sericite). Locally (e.g., in Drosh-Shishi areas), the Gawuch Formation contains several Early Eocene (40–45 Ma) dioritic to granodioritic intrusions and sills that belong to the Lowari pluton of the Kohistan batholith (cf. Tahirkheli et al., 2012). Previous studies in the study area present geochemical characteristics of the ore minerals and their host rocks (Tahirkheli et al., 2012; Farhan et al., 2021b), results from fluid inclusion investigation (Tahirkheli et al., 1996), and ages of the ore-forming processes (Tahirkheli et al., 1997). However, petrographic and mineral-chemical details that could lead to the proper characterization of the deposit and identification of the source(s) of mineralizing fluid(s) are currently lacking.

In this paper, we attempt to establish the alteration types and ore mineralogy and discuss and understand the source(s) of mineralization through systematic field observations, a detailed petrographic examination and thorough mineral-chemical and isotope investigation.

2. Geological settings

Geotectonically, the northern region of Pakistan is divided into three domains: the Kohistan-Ladakh Island Arc (K-LIA) lies between the Karakoram/Eurasian plate in the north and the Indian plate in the south (Fig. 1). The Kohistan Island Arc (KIA) is demarcated by two suture-scale faults, i.e., the Main Karakoram Thrust (MKT) or Shyok Suture Zone (SSZ) to the north and the Main Mantle Thrust (MMT) or Indus Suture Zone (ISZ) to the south (Pudsey et al., 1985; Fig. 1A; Coward et al., 1986; Petterson, 2010; Ullah et al., 2022a; Ullah et al., 2022b). A complete cross-section of the KIA has been exposed with its partial subduction beneath the Eurasian terrane and obduction onto the Indian terrane (Khan et al., 1997; Bignold and Treloar, 2003; Bignold et al., 2006). The KIA is comprised of plutonic and volcanic rocks ranging from felsic to ultramafic composition (Searle et al., 1999; Petterson, 2010).

The research area lies along the north-western boundary of KIA in district Chitral, northern Pakistan (Fig. 1B). The ore bodies are mainly hosted in the Cretaceous Gawuch Formation, which consists of metamorphosed island arc andesite-basalt and intercalations of metasediments such as quartzites and marble. Towards the south, rocks of the Gawuch Formation are intruded by the dioritic-granodioritic rocks of the Kohistan batholith. The contact zone is strongly sheared and regionally metamorphosed (Tahirkheli et al., 1997; Tahirkheli et al., 2005). The metavolcanics and marble of the upper part of the Gawuch Formation are injected by dioritic and granodioritic sills and quartz veins. The Gawuch metavolcanics are, at places, serpentinized and contain abundant ramifying quartz and carbonate micro veins. Marble overlies the metavolcanic and a severely sheared and oxidized zone marks the volcanic-marble contact.

Polymetallic sulfide mineralization occurs primarily in quartz veins and includes pyrite, fahlore, chalcopyrite, galena and magnetite. These veins are milky white in color and range in length from 1 mm to 35 cm and in width from 0.5 mm to 15 cm. The sulfide phases are found in the interstices of quartz as coarse-grained irregular masses (Tahirkheli et al., 1996). The sericitic and chloritic alterations are commonly associated with quartz veins. The majority of orebodies are fracture and fault-controlled, occurring as vein or lenticular bodies with Cu and Au contents ranging from 1 to 6 wt% and 1.5 to 1.81 ppm, respectively (Tahirkheli et al., 2012; Farhan et al., 2021b). Results from previously conducted fluid inclusion studies revealed that the ore-bearing quartz veins formed from moderate to high (12.28–13.4 wt% $NaCl_{equiv.}$) salinity fluid (Tahirkheli et al., 1996). Additionally, the lead-isotope data indicate that the minimum age of mineralization is ~42 Ma, which is relatively younger than the host Cretaceous rock (Tahirkheli et al., 1997) but similar to that of the Lowari pluton (Ar-Ar age; 40–45 Ma) of diorite and granodiorite composition (Zeitler, 1985; Tahirkheli et al., 2005).

3. Analytical methods

Three vein systems, including two barren and one ore-bearing quartz veins, were discovered at Kaldom Gol. The investigated grab samples were collected from the ore-bearing quartz veins, the Gawuch metavolcanic host rocks and the associated alteration zones. Major and trace element compositions of pyrite, fahlore, and chalcopyrite were determined by utilizing EPMA and LA-ICP-MS techniques. The sulfides were analyzed for major elements in polished sections using the JEOL JXA-8100 instrument at the Key Laboratory of Submarine Geosciences, The 2nd Institute of Oceanography, China. The analytical conditions for the EPMA consisted of 1 nA beam current, 5 μm spot diameter, and 20 kV acceleration voltage. Pure Co, Sb, and Au and pyrite, chalcopyrite, galena, sphalerite, pentlandite and gallium arsenide were used as the EPMA standards.

The trace element spot analyses of sulfides were carried out at the Christian-Albrechts University of Kiel, Germany, using a 193 nm ArF excimer laser ablation system (GeoLasPro Plus, Coherent) coupled to an Agilent 7500 s ICP-MS. The polished sections were placed in a low-dispersion, high-capacity Zurich-type laser ablation cell and cleaned with 1.0 l min^{-1} of He as carrier gas. The operating conditions comprised 8 Hz laser frequency, 6 J/cm^2 laser beam energy and 32–40 μm spot diameter. The data acquisition intervals were 20 s, sample ablation 40–50 s, and washout time 30 s.

In-situ sulfur isotope analyses were carried out using a coherent 193 nm excimer laser ablation system (GeoLasHD) coupled with a laser ablation multi-collector inductively coupled plasma mass spectrometer (LA-MC-ICP-MS) at the Wuhan Shangpu Analysis Technology, China. Helium was used as the sample carrier gas at a 600 ml/min flow rate and mixed with argon (850 ml/min) before the sample was carried into the ICP torch. The energy fluence, spot diameter, pulse frequency, number of pulses, and integration time were set to 5 mJ/cm^2, 44 μm, 2 Hz, 90 and 1.023 s, respectively. The Neptune Plus was equipped with nine Faraday cups and 1011 Ω resistors. These cups were used to collect ^{32}S and ^{34}S in a static mode. To increase signal strength, the new X skimmer cone and Jet sample cone in Neptune Plus were used. Nitrogen was added at a rate of 4 ml/min to counter the effects of polyatomic interferences. To account for instrumental mass fractionation, a standard sample bracketing (SSB) method was used. A pyrite standard PPP-1 was used as reference material to avoid matrix effects. Additionally, in-house pyrite (SP-Py-01; δ^{34}SV-CDT = 2.0 ‰ ± 0.5 ‰), chalcopyrite (SP-CP-01;

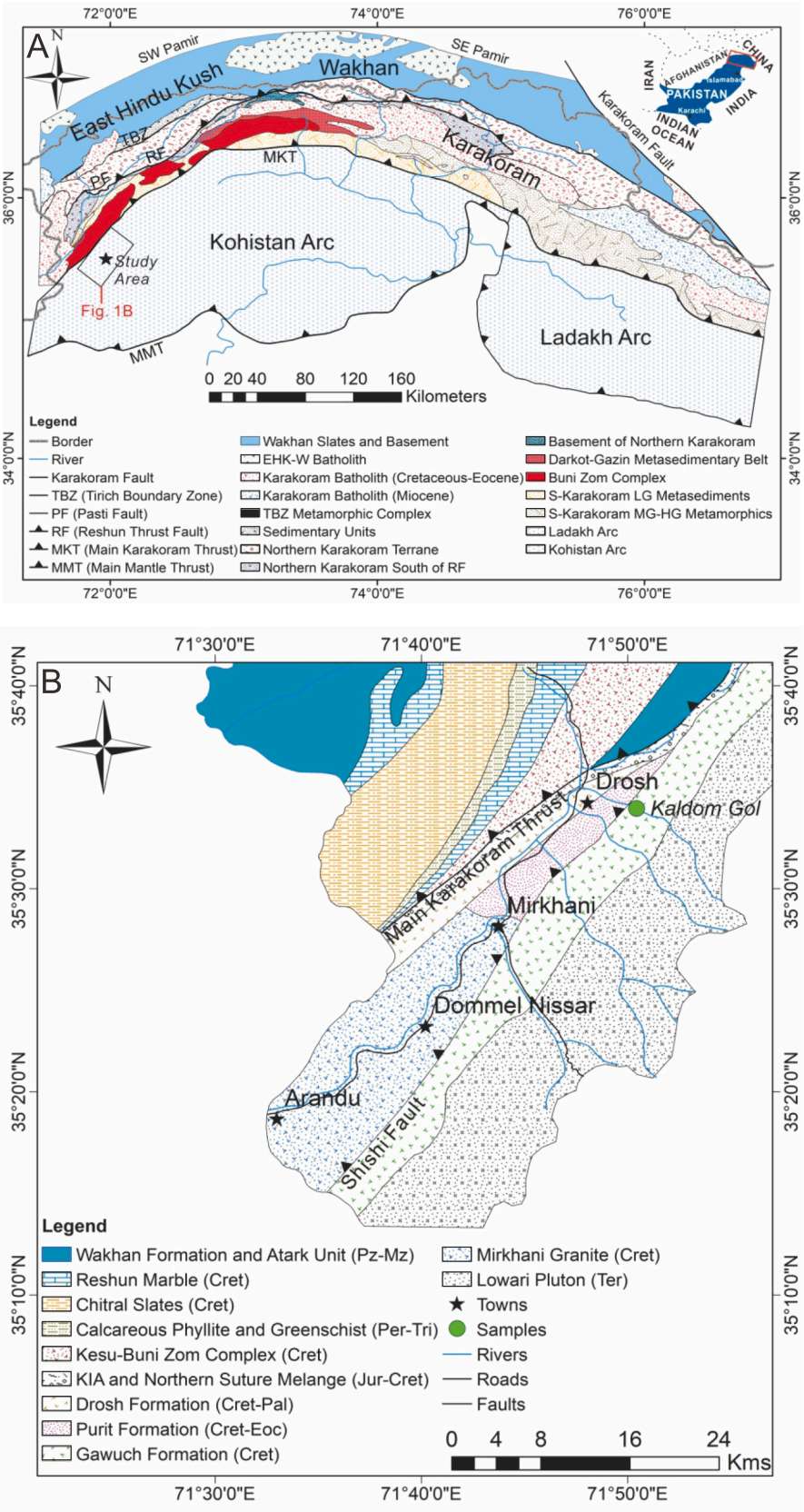

Fig. 1. Geological map of northern Pakistan (adapted from Calkins et al., 1981; Pudsey et al., 1985; Zanchi and Gaetani, 2011). The study area is distinguished by a rectangle covering the northern section of the Pakistan sketch map in the top right corner; (B) geological map of the study area (modified from Calkins et al., 1981; Pudsey et al., 1985; Zanchi and Gaetani, 2011). Cret = Cretaceous, Eoc = Eocene, Jur = Jurassic, Mz = Mesozoic, Pz = Paleozoic, Ter = Tertiary.

δ^{34}SV-CDT = 5.5 ‰ ± 0.3 ‰) and pyrrhotite (SP-Po-01; δ^{34}SV-CDT = 1.4 ‰ ± 0.4 ‰) were used continuously as unknown samples to verify the accuracy of the calibration.

For carrying out XRD analysis of clay minerals, samples were crushed to <230 μm mesh size. For pyrite and chalcopyrite samples, grains were hand-picked using a binocular microscope. They were also crushed. Gravity and evaporation methods were used for clay mineral separation (e.g., Mackenzie and Farquharson, 1956; Brindley and Brown, 1980; Ramachandran and Beaudoin, 2000). The clay samples were glycolated (Brunton, 1955; Brown and Farrow, 1956; Mosser-Ruck et al., 2005; Fonseca et al., 2010) to identify expanding clays (if present). A paste of the sample, obtained by mixing a few drops of distilled water with a small portion of the sample, was put on a glass slide and allowed to get dried. All samples were analyzed separately with a Rigaku D/Max 2550 X-ray Diffractometer (Japan) to obtain XRD spectra using Cu Kα radiation (λ = 0.15418 nm) at 450 mA and 60 kV through the 5–80° angle range, as explained by Ai et al. (2019). The preparation of different samples helped identify clay, gangue, and mineral inclusions in pyrite and chalcopyrite.

4. Results

4.1. Petrography

The Gawuch metavolcanics at Kaldom Gol are mostly altered (Fig. 2A). Fresh rocks with their original volcanic textures are scarce (Fig. 2B). These metavolcanics are extensively dissected by quartz and calcite veins (Fig. 2B). The metavolcanics display porphyritic texture and are mainly composed of plagioclase phenocrysts, hornblende and quartz (Fig. 2C–D). The secondary minerals include chlorite and epidote (after hornblende) and minor amounts of clay (illite/sericite).

Plagioclase grains are mostly turbid due to extensive replacement, mainly by epidote and clay minerals, representing saussuritization (Fig. 2C–D). Prismatic to tabular green amphibole exists as both phenocryst and groundmass (Fig. 2D, E). Amphibole is also replaced by medium-grained patches of green chlorite (Fig. 2C, E, F). Quartz is primarily fine-grained and occurs mostly in the groundmass. Secondary minerals include quartz, epidote, chlorite and sericite (Fig. 2C–F). Quartz also forms a minor fraction of the phenocrysts (Fig. 2C, D),

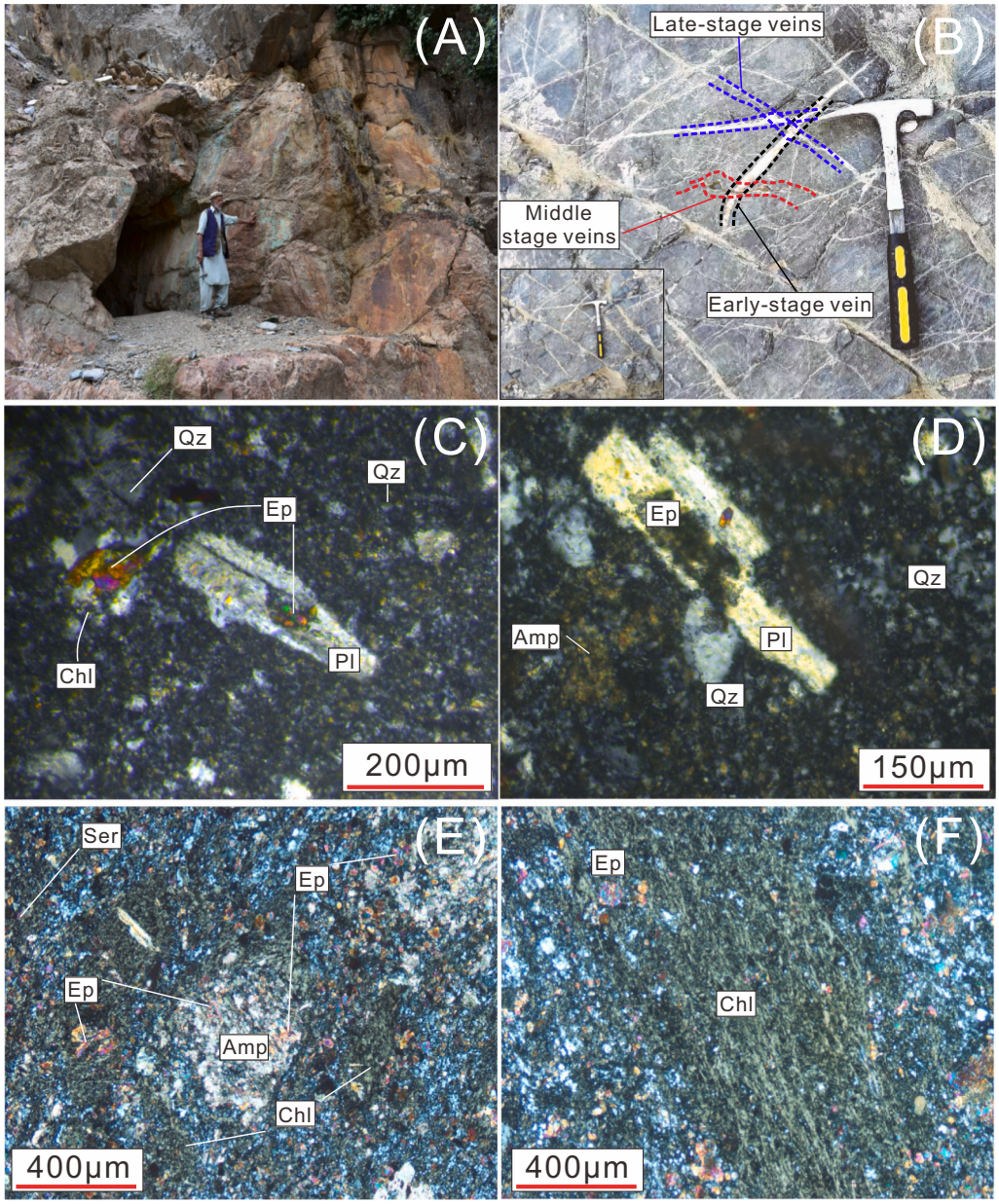

Fig. 2. Metavolcanics of Gawuch Formation. (A) Altered metavolcanic rocks; (B) Least altered metavolcanic rocks cut by three veins systems: Early, Middle and Late stages demarcated by black, red and blue dashed lines; (C) plagioclase altered to epidote surrounded by fine-grained quartz; (D) Phenocyrstic quartz; (E) Fine-grained sericite and tabular amphibole (partially transformed into epidote and chlorite); (F) Chlorite and epidote completely replacing amphibole. Adu = adularia, Amp = amphibole, Ang = anglesite, Chl = chlorite, Ccp = chalcopyrite, Cov = covellite, Ep = epidote, Fh = fahlore, Lim = limonite, Mag = magnetite, Mlc = malachite, Pl = plagioclase, Py = pyrite, Qz = quartz, Ser = sericite. (For interpretation of the references to color in this figure legend, the reader is referred to the web version of this article.)

commonly intermixed with epidote and chlorite. Epidote is primarily fine-grained and occurs as anhedral granular aggregates formed by the replacement of plagioclase and amphibole (Fig. 2C–F).

Numerous multidirectional quartz veins intrude the metavolcanics along fractures and fissures (Figs. 2B, 3A, D). These veins range in length from 1 mm to >35 cm and are about 0.5 mm to 15 cm thick (Figs. 2B, 3A, D, H, J, 4I, J). The mutually cross-cutting relationships suggest three different generations of quartz ± calcite veins (Fig. 2B); whereas the early and late-stage quartz ± calcite veins are barren, the middle-stage quartz veins are mineralized and formed as a result of the ore-forming hydrothermal activity. The mineralized quartz veins are further subdivided into Type I (a, b) and Type II based on their textures and mineral assemblages (as discussed later). These mineralized quartz veins are surrounded by two mineralogically distinct alteration zones: (1) quartz-sericite zone (Fig. 3A–C) and (2) sericite-chlorite zone (Fig. 3D–F).

4.1.1. *Quartz-sericite zone*

Quartz-sericite alterations are generally associated with Type Ia and Type Ib. In addition to abundant quartz and sericite, this zone contains minor amounts of chlorite (Fig. 3A–C). Quartz typically coexists with sericite as a fine-grained, recrystallized variety (Fig. 3B, C). This textural relationship may have resulted from silicification whereby the silica released through sericitization of plagioclase precipitated as quartz. That is why sericite and quartz frequently occur within and occasionally pseudomorph phenocrysts of plagioclase (Fig. 3B, C).

4.1.2. *Quartz-sericite-chlorite zone*

Sericite-chlorite alteration zone is mainly associated with Type II mineralization. This zone is mainly composed of quartz, sericite and chlorite, which are formed by the replacement of plagioclase and amphibole (Fig. 3D–F). Dark green chlorite (Fig. 3D, E) and off-white sericite occur in the vicinity of quartz veins (Fig. 3D, E).

4.2. *Mineralized quartz vein*

Generally, the principal middle-stage quartz veins consist of chlorite, sericite/illite, adularia (rare) and bladed calcite, pyrite, fahlore, chalcopyrite and galena and minor amounts of magnetite (Figs. 3A–O,

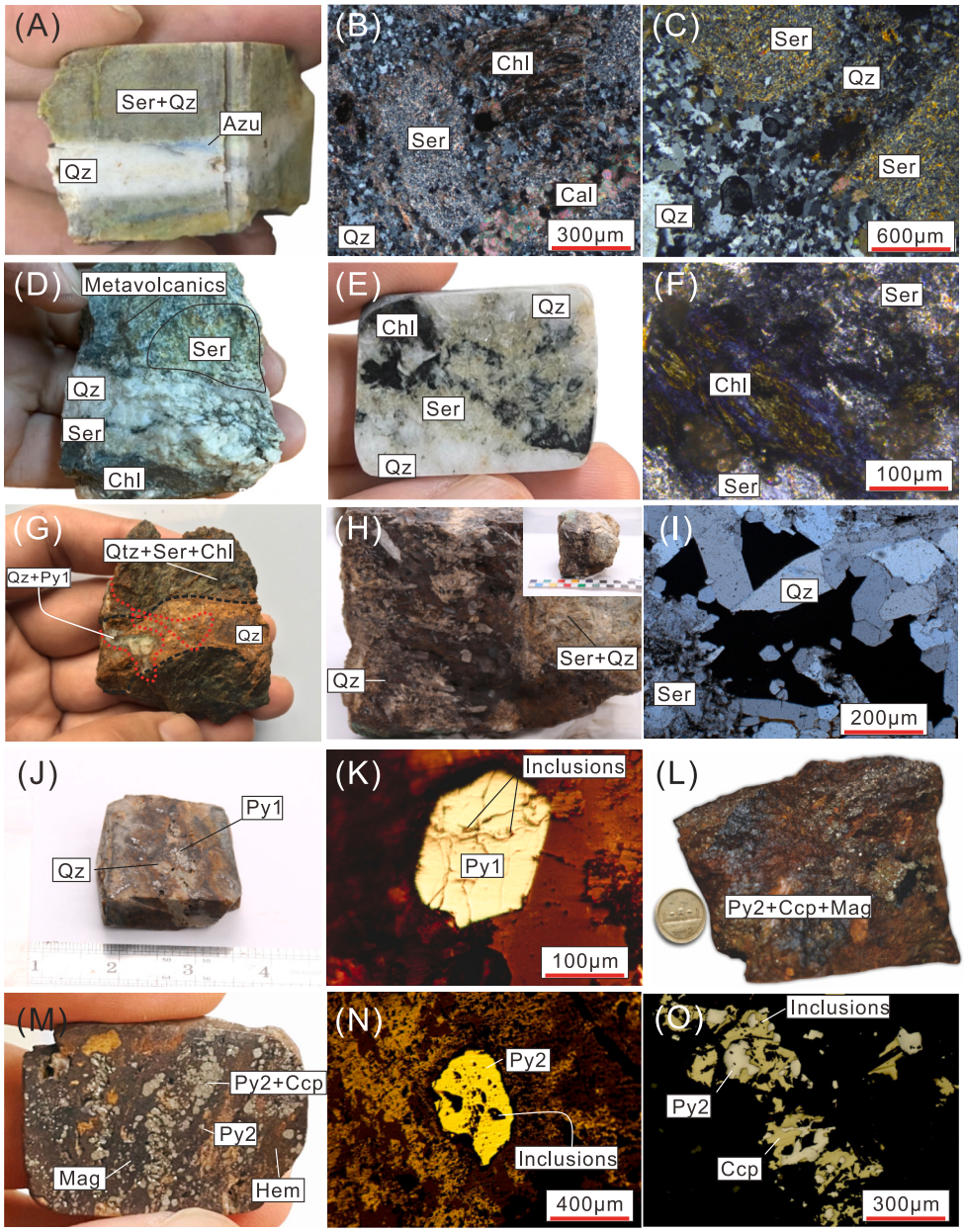

Fig. 3. (A–C) Quartz-sericite alteration zones, (D–F) sericite-chlorite alteration, (G–O) Type I mineralization associated with quartz veins; (A) hand specimen, (B) photomicrograph shows sericite and chlorite replacing plagioclase and amphibole, (C) cross-polarized light photomicrograph displays plagioclase pseudomorphic texture at top right end; (D and E) hand specimens, (F) cross-polarized light photomicrographs illustrating medium-grained dark green chlorite and fine-grained white sericite replace amphibole and plagioclase; (G-K) Type Ia mineralization associated with quartz veins; (G) hand specimen showing early formed quartz vein intersected by mineralized quartz veins; (H) hand specimen exhibits euhedral quartz (comb texture); (I) cross-polarized light photomicrograph shows comb texture; (J) hand specimen displays quartz and Py1 mineralization; (K) reflected light photomicrograph illustrates euhedral Py1; (L–O) Type Ib mineralization associated with quartz veins (L and M) hand specimens of pyrite, chalcopyrite and magnetite-bearing samples; (N) reflected light photomicrograph displays Py2 mineralization; (O) reflected light photomicrograph displays chalcopyrite and Py2 with mutually interstitial relationship. (For interpretation of the references to color in this figure legend, the reader is referred to the web version of this article.)

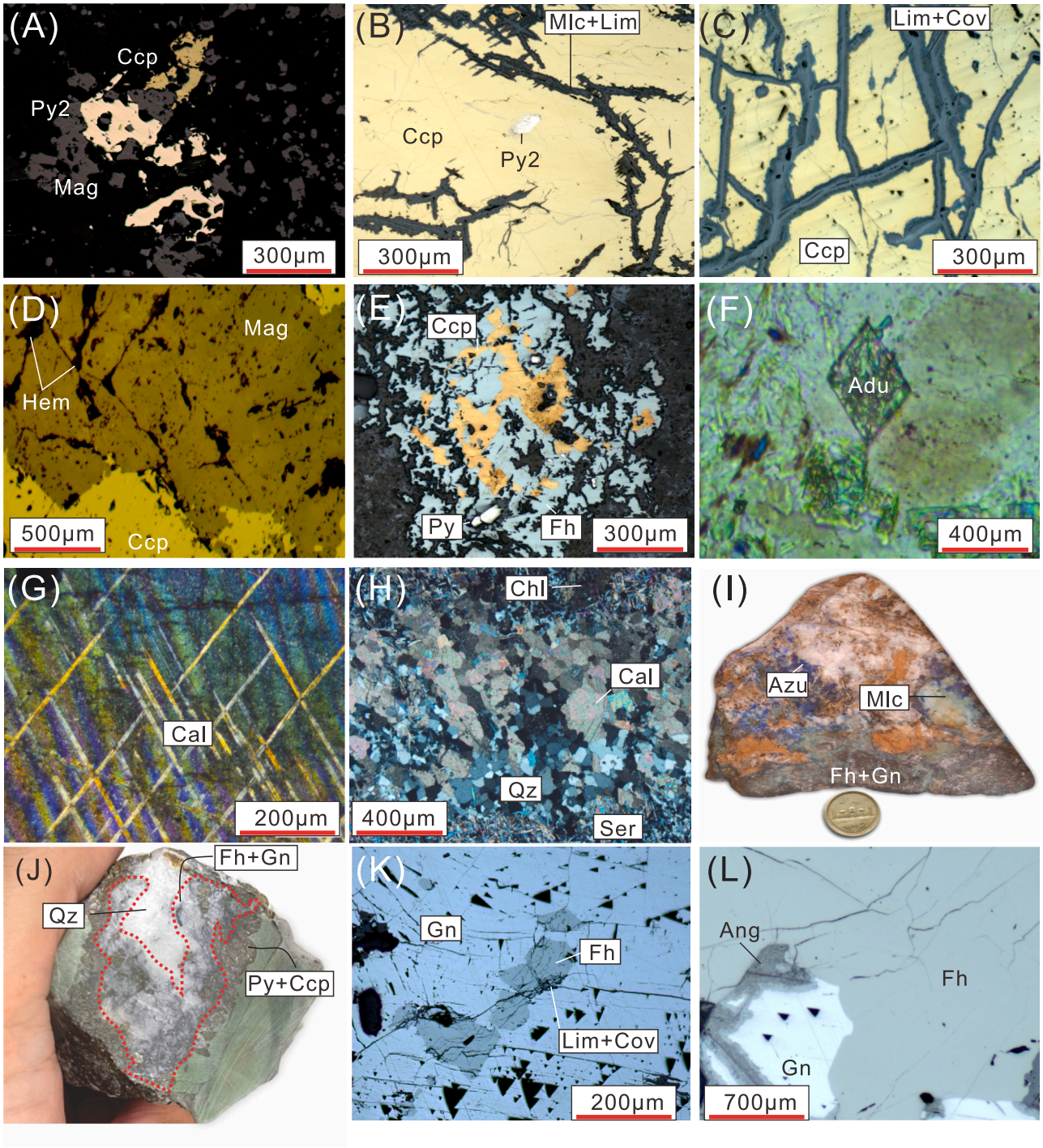

Fig. 4. (A–D) Type Ib mineralization; (A) reflected light photomicrograph of chalcopyrite, pyrite and magnetite showing interstitial relationship with each other; (B) reflected light photomicrograph exhibits the replacement of chalcopyrite by malachite mixed with limonite; (C) reflected light photomicrograph illustrates the replacement of chalcopyrite by limonite-covellite mixture; (D) magnetite is replaced by hematite (E–L) Type II mineralization; (E) fahlore from Type II replaces chalcopyrite and pyrite from Type I; (E–H) gangue minerals associated with Type II mineralization (E) cross-polarized refracted light photomicrograph displays rhombic adularia; (G) cross-polarized refracted light photomicrograph illustrate bladed calcite; (H) cross-polarized photomicrograph exhibits quartz mosaic texture; (I) hand specimens of fahlore and galena bearing sample; (J) hand specimen shows fahlore and galena from Type II replacing pyrite and chalcopyrite (Type I); (K) reflected light photomicrograph demonstrates the coexistence of galena and fahlore; (L) anglesite replaces galena.

4A–L). The vein quartz exhibits comb and mosaic textures (Figs. 3H, I, 4H). The secondary minerals, which include malachite, limonite, azurite, hematite, anglesite and covellite, represent products of supergene alteration (Figs. 3A, M, 4B–D, I, K, L).

Two sets of ore samples representing Type I and Type II of the mineralization from the middle-stage quartz veins were selected for a detailed mineral-chemical investigation during the current study. Type I is further subdivided into Type Ia and Type Ib. Type Ia is dominated by quartz showing comb texture, sericite and chlorite, while ore minerals include pyrite (Fig. 3G–K), while Type Ib contains pyrite, chalcopyrite and magnetite (Figs. 3L–O, 4A–D). Pyrite is the most common ore mineral in Type Ia and Type Ib. Two textural types of pyrite, namely Py1 and Py2, were distinguished. Py1 is medium to coarse-grained (50–2000 μm), euhedral to subhedral and occurs in Type Ia

(Fig. 3G–K). It is usually associated with euhedral quartz. Py1 usually forms interstitial textures with silicate minerals and also occurs as disseminated grains (Fig. 3K).

Py2 is anhedral and medium-grained (50–1500 μm) and occurs in Type Ib (Figs. 3L–O, 4A). It occupies the interstices among silicate minerals and is commonly associated with chalcopyrite and magnetite (Figs. 3N, O, 4A). Grains of both pyrite types host mostly quartz inclusions; however, the inclusions in Py2 are more abundant (Fig. 3K, N; Supplementary data S3).

Chalcopyrite is associated with Py2 and magnetite in Type Ib. It is medium-grained (50–1500 μm), irregularly shaped and occurs as disseminated grains within quartz veins and also exhibits an interstitial relationship with Py2 (Figs. 3O, 4A). The grains of chalcopyrite contain abundant inclusions of quartz (Figs. 3O, 4A; Supplementary data S3). Chalcopyrite is replaced by malachite + limonite and limonite + covellite mixtures (Fig. 4B, C). Magnetite is tinted greyish in reflected light and occurs as anhedral to subhedral grains. Interstitial irregular magnetite grains contain rounded to subrounded silicate mineral inclusions (Fig. 4A). It is most frequently found in association with Py2 and chalcopyrite. Magnetite is typically replaced by hematite (Fig. 4D).

Type II is dominated by fahlore and galena, while gangue minerals include bladed calcite, mosaic quartz, chlorite, minor sericite and rhombic adularia (Fig. 4E–L). Fahlore is the most abundant Cu-bearing phase in Type II (Fig. 4I–L) and occurs as irregular, coarse-grained masses generally occupying interspaces and filling fractures within grains of silicate phases. Fahlore also encloses silicate minerals, mainly quartz and replaces chalcopyrite and pyrite (Fig. 4E). Limonite + covellite and supergene malachite and azurite also replace fahlore grains (Fig. 4I, K).

Grains of galena are typically medium to large sized, anhedral to subhedral, and display characteristic triangular pits (Fig. 4K, L). Galena is frequently associated and intergrown with fahlore. Locally, fahlore is commonly encrusted by galena (Fig. 4K); however, the opposite relation is also noticed (Fig. 4L). Galena has been replaced by anglesite (Fig. 4L) and limonite + covellite along fractures (Fig. 4K).

4.3. Sulfide chemistry

Iron and S contents (wt%) in Py1 (13 spots) are 45.07–46.21 and 53.21–54.21, respectively (Table 1 and Table S1). Py1 generally shows a wide range of concentrations (ppm) for trace elements such as As (303–10,203), Cu (1–3800), Co (22–445), Ni (18–410), Se (54–251), Bi (4–75) and Au (0.01–3), whereas Sb (0.3–3), Ag (0.04–1.7) and Cd (bd.–1) display less variability (Table 1, Fig. 5). Ruthenium, Rh, Pd, Te, Ta, Ir, Pt, and Hg are generally below their detection limits (Table S2).

In the analyzed Py2 crystals, Fe and S contents (wt%) vary as follows: 45.98–47.06, and 52.94–53.56, respectively. Chemically, Py2 is generally more homogenous than Py1. However, limited variation is observed in the concentrations (ppm) of Co (28–478), Ni (11–239), Cu (9–185), Bi (21–169), Pb (6–69), Zn (1–35), Sb (1.5–7), Cr (0.6–6), Cd (bd. − 0.5) and Au (0.04–0.02), whereas As (78–2448) shows wide variation. Excluding the inclusion analyses (Table 1, Fig. 5), the average contents of Cu, Zn, As, Sb, Cr, Mn, Ni, Se, Ag, Au, Pb and Bi are generally higher in Py2 than in Py1.

Eighteen spots on fahlore were analyzed for their major, minor and trace element contents (Table 1 and Table S1). Copper, S, Sb, As and Zn contents (in wt%) vary as follows: 36.76–42.31, 22.83–26.07, 16.07–18.63, 7.15–9.06 and 7.91–9.48, respectively. Iron, Ag and Cd represent minor constituents, with contents (wt%) ranging from 0.63 to 1.04, 0.5 to 0.6, and 0.2 to 0.4, respectively. Due to elevated Zn content, the fahlore is characterized as zincian tetrahedrite. Mercury, Co, Ni, Pb, Mn, Ba and Te contents (in ppm) vary as follows: 429–972, 52–81, 5–860, 0.3–25, 9–11 and 6–11, respectively. Selenium, Rh, Ir, and Pt are below their detection limits, whereas Y, Zr, Mo, Sn, Cs, Hf, Ta, W and U rarely exceed ppm levels. The concentrations (ppm) of Pd and Au are 5.1–7 and 0.01–2.1, respectively.

EMPA analysis (Table S1, $n = 12$) of chalcopyrite shows near-stoichiometric chemistry ($Cu_{1.0}Fe_{1.0}S_{1.9}$). Chalcopyrite displays high concentrations (ppm) of As (10–12), Se (58–59), Y (12–13), Zr (13–21), Ag (19–22) and Sn (10–11). Relatively low concentrations (ppm) are noticed for Co (0.05–0.6), Ni (0.06–11), Zn (4.5–6), Sr (0.4–0.7) and Cd (1.9–2). Gold ranges from 0.09 to 0.11 ppm, while Te, Cs, Hf, Ta, Tl and Bi are mostly below 1 ppm. Molybdenum and Pb contents (ppm) fall in the ranges of 0.24–1 and 80–183, respectively. Fig. 5 illustrates trace element ranges for Py1 ($n = 13$), Py2 ($n = 6$), fahlore ($n = 18$), and chalcopyrite (n = 12). Lead and S contents (in wt%) of galena are 86.65 and 12.66, respectively. The average contents of Cu, Zn, Sb and Cd are below the detection level. Small but significant amounts of Fe, As and Ag are also present with average concentrations (wt%) of 0.01, 0.05 and 0.01, respectively.

A total of 14 in-situ sulfur isotope measurements were made on pyrite from Kaldom Gol (Table 2). The $\delta^{34}S$ values (in ‰) exhibit a narrow range for both Py1 (−0.58 to +2; averaging +1.01) and Py2 (−0.24 to +2.03; averaging +1.32).

5. Discussion

5.1. Mineral inclusions and solid solutions

A variety of elements, including As, Au, Cu, Co, Ni, Ag, Te, Pb and Se can be accommodated in pyrite through substitution for its essential components, i.e., Fe and S (e.g., Abraitis et al., 2004; Reich et al., 2005; Zhang et al., 2014; Morishita et al., 2019; Ishida et al., 2022; Zhou et al., 2022). Previously, it has been found that pyrite may contain considerable amounts (in wt%) of As (up to 9.6) and Co (up to 5.61), while minor concentrations (in wt%) of Sb (0.7), Au (0.3) and Ni (0.7) in its lattice (Abraitis et al., 2004; Giri et al., 2018). Similarly, Cu, Ag, and Pb may also occur as trace elements in the pyrite lattice; more frequently, however, these elements occur as discrete mineral inclusions (Abraitis et al., 2004; Zhang et al., 2014; Zhou et al., 2022).

The As shows a strong negative correlation with S in Py1, suggesting that it is substituted for S (Fig. 6A). The smoothness of the time-resolved spectra for As supports this conclusion (Fig. 7A, B). Although the negative correlation of As with S in Py2 is comparatively poor (Fig. 6A), the time-resolved spectra for As profile is smooth (Fig. 7C, D). We, therefore, interpret that As is present in solid solution. The weak correlation between As and S in Py2 may be partly because the amount of data on Py2 is limited. A moderate negative correlation is observed between Se and S in both Py1 and Py2, suggesting Se substitution for S (Fig. 7B). The entrance of As into the pyrite lattice causes ionic imbalance and structural distortion, thus allowing the entry of other trace elements (e.g., Cu, Ni, Co, Ag, and Au) into the pyrite structure (e.g., Deditius et al., 2014). Moderate to strong negative correlations are observed between Fe and Au in both the Py1 and Py2, suggesting that the latter metal entered in pyrite structure through isomorphous substitution (Fig. 6C). Time-resolved depth profiles of Au show both smooth and spiky profiles implying Fe ↔ Au substitution and the existence of Au as micro-inclusions, respectively (Fig. 7A–D). The spectra for Ni and Co are smooth, suggesting their occurrence in the crystal lattice of Py1 and Py2 (Fig. 7A–D).

Copper and Zn show poor or no correlation with Fe (Fig. 6D). However, Cu exhibits a strong positive correlation with Zn in Py1 and Py2 (Fig. 6E). Moreover, there are Cu and Zn spikes in time-resolved spectra (Fig. 7A–D). Therefore, these elements are mostly present as inclusions such as chalcopyrite and sphalerite (e.g., Baidya et al., 2020). The positive correlation of Ag with Fe suggests a lack of Ag ↔ Fe substitution (Fig. 6F). The rough spectrum for Ag also proves its existence as an inclusion rather than a substituent cation in pyrite (Fig. 7A–D). Antimony, together with Bi, can enter into the crystal lattice of galena through substitution for Pb (Li et al., 2016; Shao et al., 2018; Baidya et al., 2020). Good positive correlations of Pb with Sb and Bi in both P1 and Py2 imply the presence of galena inclusions in Py1 and Py2

Table 1
EPMA and LA-ICP-MS analyses of sulfides from Kaldom Gol. Major elements are presented in wt%, while trace elements are shown in ppm. For pyrite (Py1 and Py2), fahlore (Fh), and chalcopyrite (Ccp), the major elements include Fe and S, Fe, S, Cu, Zn, As, and Sb, and Fe, S and Cu, respectively. Detection limits (DL) are presented in % for major elements, while ppm for trace elements.

Mineral type	DL	Py1	Py1	Py1	Py1	Py1	Py1	Py1	Py1
Spot point		Py1-60	Py1-62	Py1-63	Py1-64	Py1-65	Py1-66	Py1-67	Py1-68
S	0.003	53.24	53.81	53.93	53.88	53.98	53.98	54.21	53.81
Fe	0.009	45.07	46.14	45.62	45.36	46.22	45.14	45.58	45.14
Cu63	0.004	1.46	3800.17	75.99	2.84	1.94	2.80	2.44	1.73
Zn66	0.017	0.99	14.23	6.52	1.63	3.34	8.79	3.05	1.25
Pb208	0.059	0.83	5.07	15.02	6.46	11.46	15.66	15.81	7.80
As75	0.207	10,203.23	1937.75	743.41	1097.62	610.89	575.92	303.55	1953.19
Sb121	0.000	0.29	1.84	1.69	0.89	1.42	1.95	1.50	1.48
Co59	0.010	225.20	90.30	150.58	228.82	189.80	430.22	328.17	100.80
Ni60	0.050	78.89	142.52	52.52	35.65	18.46	68.86	20.11	55.80
Se77	5.000	190.55	148.54	88.99	89.02	59.84	112.26	53.61	131.18
Mo98	0.010	0.28	0.09	0.03	0.04	0.09	0.52	0.80	0.39
Ag109	0.050	<0.05	1.15	0.09	0.05	<0.05	0.05	<0.05	0.14
Te125	0.010	<0.01	<0.01	<0.01	<0.01	<0.01	<0.01	<0.01	<0.01
Au197	0.005	2.97	0.13	0.03	0.04	0.02	0.02	0.03	0.06
Bi209	0.050	4.13	18.97	50.25	23.31	43.32	54.36	50.01	22.10

Mineral type	DL	Py1	Py1	Py1	Py1	Py1	Py2	Py2	Py2
Spot point		Py1-70	Py1-72	Py1-61	Py1-69	Py1-71	Py2-54	Py2-56	Py2-57
S	0.003	53.92	53.51	53.78	54.01	53.87	52.94	53.56	53.56
Fe	0.009	45.60	45.12	45.09	45.22	45.20	46.79	47.06	47.00
Cu63	0.004	20.25	5.07	3.44	11.97	1.69	185.02	28.21	8.99
Zn66	0.017	3.11	1.22	1.87	5.54	0.62	35.75	20.24	2.31
Pb208	0.059	32.39	2.67	1.87	14.06	5.47	35.07	9.95	5.90
As75	0.207	1010.51	4360.35	2103.12	555.82	1179.06	1947.65	77.99	2448.27
Sb121	0.000	2.99	0.78	0.94	1.55	1.66	4.98	2.41	1.50
Co59	0.010	180.54	54.77	21.93	445.12	218.41	395.91	66.09	37.52
Ni60	0.050	77.02	410.65	179.63	37.42	99.98	239.69	11.50	44.79
Se77	5.000	251.03	126.50	175.69	56.70	158.12	228.43	200.54	111.97
Mo98	0.010	4.15	0.69	0.06	0.07	0.93	46.18	1.78	0.19
Ag109	0.050	1.72	<0.05	<0.05	0.06	<0.05	3.13	4.22	0.16
Te125	0.010	<0.01	<0.01	<0.01	<0.01	<0.01	<0.01	<0.01	<0.01
Au197	0.005	0.55	0.05	0.07	0.01	0.02	0.07	0.05	0.13
Bi209	0.050	75.35	11.57	10.76	42.45	17.55	58.12	38.73	20.96

Mineral type	DL	Py2	Py2	Py2	Fh	Fh	Fh	Fh	Fh
Spot point		Py2-59	Py2-55	Py2-58	Fh-73	Fh-74	Fh-75	Fh-76	Fh-77
S	0.003	53.41	53.43	52.99	25.93	24.90	24.22	24.01	23.05
Fe	0.009	45.99	46.79	46.94	0.77	0.77	0.63	1.04	0.69
Cu63	0.004	10.02	19.23	23.44	40.46	40.31	38.91	38.97	39.78
Zn66	0.017	6.18	1.86	1.33	7.91	8.61	8.59	8.31	8.82
Pb208	0.059	63.50	11.17	69.19	12.77	9.13	6.22	351.35	5.81
As75	0.207	2104.78	158.49	2188.82	8.57	9.06	8.46	8.83	8.72
Sb121	0.000	7.45	2.67	2.64	17.05	16.07	17.62	16.25	16.28
Co59	0.010	116.36	477.83	27.91	52.06	54.86	57.48	59.53	63.39
Ni60	0.050	237.36	98.29	77.31	<0.05	<0.05	< 0.05	1.99	<0.05
Se77	5.000	135.25	128.07	158.85	<5	<5	<5	<5	<5
Mo98	0.010	0.06	10.16	0.04	1.47	1.18	1.68	1.08	1.05
Ag109	0.050	1.08	1.54	2.89	5642.00	5770.97	6024.70	5958.17	5797.99
Te125	0.010	<0.01	<0.01	<0.01	6.75	7.22	6.32	11.33	10.79
Au197	0.005	0.23	0.18	0.23	<0.005	<0.005	<0.005	0.51	<0.005
Bi209	0.050	169.50	35.08	110.76	0.07	0.21	<0.05	<0.05	0.09

Mineral type	DL	Fh	Fh	Fh	Fh	Fh	Fh	Fh	Fh
Spot point		Fh-78	Fh-80	Fh-81	Fh-82	Fh-83	Fh-84	Fh-85	Fh-86
S	0.003	23.81	22.83	25.41	24.17	25.18	24.14	23.67	23.39
Fe	0.009	0.67	0.67	0.79	0.78	0.75	0.72	0.84	0.81
Cu63	0.004	39.27	38.51	41.15	40.77	41.33	36.75	38.86	38.10
Zn66	0.017	8.54	9.48	8.02	8.45	8.53	8.46	8.27	8.24
Pb208	0.059	5.52	6.93	8.14	12.43	6.43	14.34	60.71	9.65
As75	0.207	8.34	8.54	8.13	8.52	8.48	7.15	8.43	7.82
Sb121	0.000	17.91	17.08	17.91	17.09	17.08	18.63	17.63	18.01
Co59	0.010	64.85	54.36	81.31	77.11	74.47	70.01	76.25	80.06
Ni60	0.050	<0.05	0.06	<0.05	<0.05	<0.05	0.15	<0.05	<0.05
Se77	5.000	<5	<5	<5	<5	<5	<5	<5	<5
Mo98	0.010	0.29	0.03	1.35	1.44	1.45	1.43	1.04	1.71

(*continued on next page*)

Table 1 (*continued*)

Mineral type	DL	Fh	Fh	Fh	Fh	Fh	Fh	Fh	Fh
Ag109	0.050	5876.90	6143.65	5541.14	5639.48	5487.00	6315.01	6043.87	6177.13
Te125	0.010	7.70	8.62	7.53	6.15	7.55	5.97	6.91	8.73
Au197	0.005	<0.005	0.01	<0.005	2.10	0.01	<0.005	0.10	<0.005
Bi209	0.050	<0.05	<0.05	0.10	0.12	0.09	0.19	0.20	0.14

Mineral type	DL	Fh	Fh	Fh	Fh	Fh	Ccp	Ccp	Ccp
Spot point		Fh-87	Fh-88	Fh-89	Fh-90	Fh-91	Ccp-202	Ccp-212	Ccp-221
S	0.003	23.96	24.88	26.07	24.85	23.04	34.47	34.47	34.45
Fe	0.009	0.79	0.69	0.67	0.74	0.71	30.39	30.50	30.23
Cu63	0.004	42.31	38.19	39.50	39.98	38.61	34.62	34.57	34.63
Zn66	0.017	8.45	8.63	8.93	8.51	8.43	4.73	4.56	4.73
Pb208	0.059	860.18	10.25	9.80	8.65	12.21	131.36	79.58	131.36
As75	0.207	9.00	8.37	8.48	8.68	8.71	10.71	11.08	10.71
Sb121	0.000	16.21	17.90	17.16	16.84	16.63	11.99	12.38	11.99
Co59	0.010	74.87	65.56	65.81	71.45	55.61	0.06	0.05	0.06
Ni60	0.050	0.13	0.10	<0.05	<0.05	<0.05	0.07	0.06	0.07
Se77	5.000	<5	<5	<5	<5	<5	58.27	58.59	58.27
Mo98	0.010	1.08	1.78	1.44	1.10	1.09	0.09	0.10	0.09
Ag109	0.050	5373.27	6164.10	5840.05	5784.80	6060.80	22.47	22.57	22.47
Te125	0.010	10.98	8.10	7.43	7.14	9.24	0.28	0.33	0.28
Au197	0.005	0.02	0.03	<0.005	0.02	0.03	0.10	0.11	0.10
Bi209	0.050	0.32	0.14	0.14	0.09	<0.05	0.49	0.48	0.49

Mineral type	DL	Ccp	Ccp	Ccp	Ccp
Spot point		Ccp-222	Ccp-232	Ccp-242	Ccp-243
S	0.003	34.49	34.40	34.45	34.46
Fe	0.009	30.28	30.16	30.42	30.51
Cu63	0.004	34.68	35.27	34.63	34.65
Zn66	0.017	4.90	5.73	4.92	4.64
Pb208	0.059	105.47	101.80	104.55	183.14
As75	0.207	10.89	12.09	11.19	10.34
Sb121	0.000	12.19	12.03	12.15	11.59
Co59	0.010	0.06	0.58	0.19	0.08
Ni60	0.050	0.07	10.63	2.71	0.08
Se77	5.000	58.43	59.03	58.58	57.95
Mo98	0.010	0.10	0.90	0.30	0.08
Ag109	0.050	22.52	18.96	21.63	22.37
Te125	0.010	0.31	0.29	0.30	0.24
Au197	0.005	0.10	0.10	0.10	0.09
Bi209	0.050	0.48	0.44	0.47	0.49

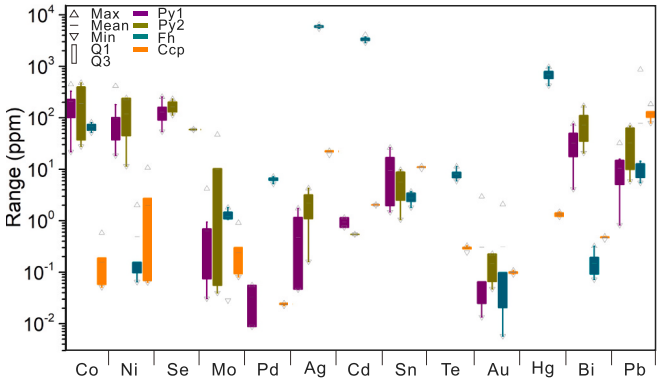

Fig. 5. Logarithmic-scaled boxplot showing the distribution of selected trace elements in main sulfides ores hosted in quartz veins at Kaldom Gol.

Table 2
LA-MC-ICP-MS S-isotopic compositions of pyrites from Kaldom Gol.

Sample name	Pyrite type	$\delta^{34}S_{V\text{-}CDT}$(‰)
KG-01	Py1	0.71
KG-01	Py1	−0.58
KG-02	Py1	0.81
KG-02	Py1	1.46
KG-03	Py1	2
KG-04	Py1	1.5
KG-05	Py1	1.2
KG-01	Py2	−0.24
KG-01	Py2	−0.05
KG-02	Py2	1.54
KG-02	Py2	2.03
KG-03	Py2	1.94
KG-04	Py2	2.04
KG-05	Py2	2.03

(Fig. 6G). The LA-ICP-MS time-resolved depth profile provides additional evidence for galena microinclusions in pyrite. The parallel spectrum of Sb and Bi to that of Pb confirms that Sb and Bi occur mainly in inclusions of galena (Fig. 7D).

Negative correlations between Cu and Ag, Zn and Fe, and As and Sb imply isomorphic substitutions in fahlore (e.g., Xu, 2005). Repstock et al. (2016) proposed the substitution of tetravalent tellurium for trivalent As and Sb in tetrahedrite, goldfieldite and Te-rich tennantite. In fahlore from Kaldom Gol, Sb exhibits strong and moderate negative correlations with As and Te, respectively, suggesting the substitution of these elements for Sb (Fig. 6H, I). The substitution of Ag for Cu is demonstrated by their significant negative correlation (Fig. 6J). Fe displays a moderate inverse correlation with Zn, implying Zn replacing Fe (Fig. 6K). Some elements, especially Pb, appear to be occurring more commonly as micro-inclusions in fahlore than others; Pb is most likely

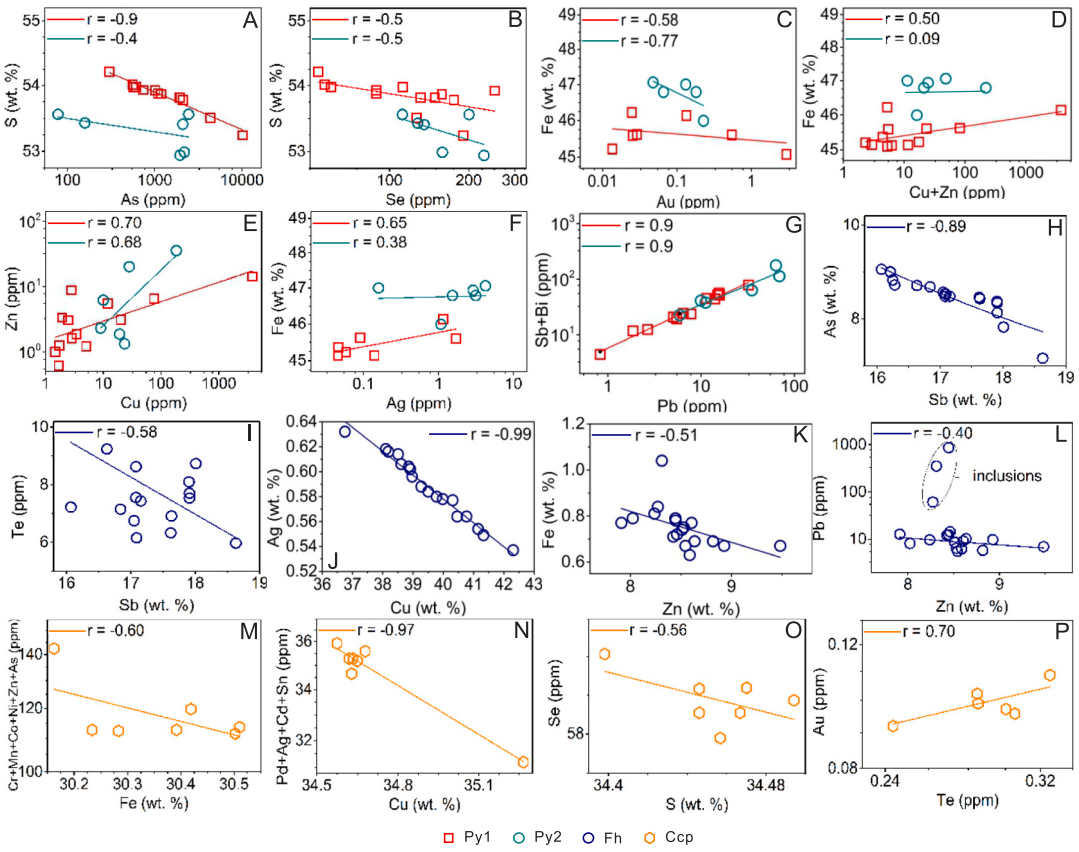

Fig. 6. Binary plots illustrating positive and negative correlations among selected trace elements analyzed using LA-ICP-MS on pyrite, fahlore and chalcopyrite from Kaldom Gol; red square symbols indicate Py1, and green circles symbols indicate Py2. (For interpretation of the references to color in this figure legend, the reader is referred to the web version of this article.)

present as galena micro-inclusions (George et al., 2017). The observed moderate negative correlation of Pb with Zn also suggests Zn ↔ Pb substitution (Fig. 6L). However, the markedly high amounts of Pb in some of the LA-ICP-MS spot analyses and spikes shown by the time-resolved depth profiles indicate the presence of galena inclusions in fahlore from Kaldom Gol (Table 1; Fig. 7G, H). The flat time-resolved depth profiles for Co, Cu, Zn, As, Pd, Ag, Cd, Sb, Te, Hg, Pb and Bi indicate their occurrence as solid solutions rather than inclusions (Fig. 7E, F). Yet, the spiky Te and Pb profiles also show the presence of tellurides and galena inclusions (Fig. 7G, H). Similarly, the rough character of the time-resolved depth profiles for Ni and Au indicates the occurrence of these metals as inclusions in fahlore (e.g., Fig. 7H).

In chalcopyrite, Cr, Mn, Co, Ni, Zn and As negatively correlate with Fe, suggesting their substitution for the latter element (Fig. 6M). The significant but negative correlation indicates the substitution of Pd, Ag, Cd and Sn for Cu (Fig. 7N). Sulfur also displays a negative correlation with Se, indicating Se^{2-} for S^{-} substitution (e.g., Huston et al., 1995) (Fig. 6O). The time-resolved depth profiles for Co, Ni, Zn, As, Se, Pd, Ag, Cd and Sb are flat, suggesting their incorporation into chalcopyrite structure (Fig. 7I, J). However, Co and Ni also show spiky time-resolved depth profiles reflecting that these two elements also occur as mineral inclusions (e.g., millerite, bravoite, vaesite, etc.; González-Álvarez et al., 2013). A strong positive correlation between Te and Au does imply the occurrence of Au-telluride inclusions in chalcopyrite (Fig. 6P). The appearance of Te, Au, Pb and Bi spikes in the time-resolved depth profiles indicates the presence of Au-tellurides and galena inclusions (Fig. 7I, J). Galena can contain Ag and Bi as solid solutions and in the form of inclusions (e.g., Shao et al., 2018). The similarity in the LA-ICP-MS time-resolved depth profiles for these two elements suggests their incorporation into galena, which exists as an inclusion in the studied chalcopyrite (Fig. 7J).

5.2. Physicochemical conditions

The trace element composition of different sulfides can be utilized to interpret the physicochemical conditions of their parent (ore-forming) fluids. By employing the Se in the pyrite geothermometer of Keith et al. (2018) and using the regression $Se_{(pyrite)} = (5 \times 10^{13}) \times T^{-4.82}$ to calculate the temperature of the ore-forming fluid, the estimated average temperatures (°C) for Py1 and Py2 from Kaldom Gol are 262 (221–304) and 244 (225–261), respectively.

Fahlore is an important ore mineral formed under high oxygen fugacity (fO_2) conditions in porphyry-related mineral systems, such as porphyry, skarn, and epithermal polymetallic deposits (e.g., Sack and Lichtner, 2009; Wei et al., 2020). Previous research has demonstrated that the high fluid fO_2 (FMQ > +1.5) (e.g., Zhang et al., 2013) is a significant factor for porphyry-related mineralization. Fahlore precipitates at temperatures between 100° and 400 °C, but predominantly between 180° and 300 °C, and at pressures <4 Kbar (Sack, 2005). Results from the fluid inclusion study by Tahirkheli et al. (1996) and temperature estimation based on the Se content of pyrite (current study) suggest a temperature range of 160–350 °C.

High temperature favors the entry of Sn into chalcopyrite and other sulfides (Maslennikov et al., 2009). The low concentration of Sn (11 ppm average) suggests a relatively low-temperature origin for the Kaldom Gol chalcopyrite. Generally, temperature controls the Cd/Zn ratio in hydrothermal chalcopyrites (George et al., 2018). Low-temperature (<400 °C) epithermal chalcopyrites usually show depletion in Cd relative to Zn. The converse is true for chalcopyrites formed at higher temperatures (>400 °C) (George, 2017). The relatively low Cd/Zn ratios (0.35–0.45) in the hydrothermal chalcopyrite from the study area indicate formation at <400 °C. In terms of Se contents (58–59 ppm), the Kaldom Gol chalcopyrite is closely similar to the low-moderate

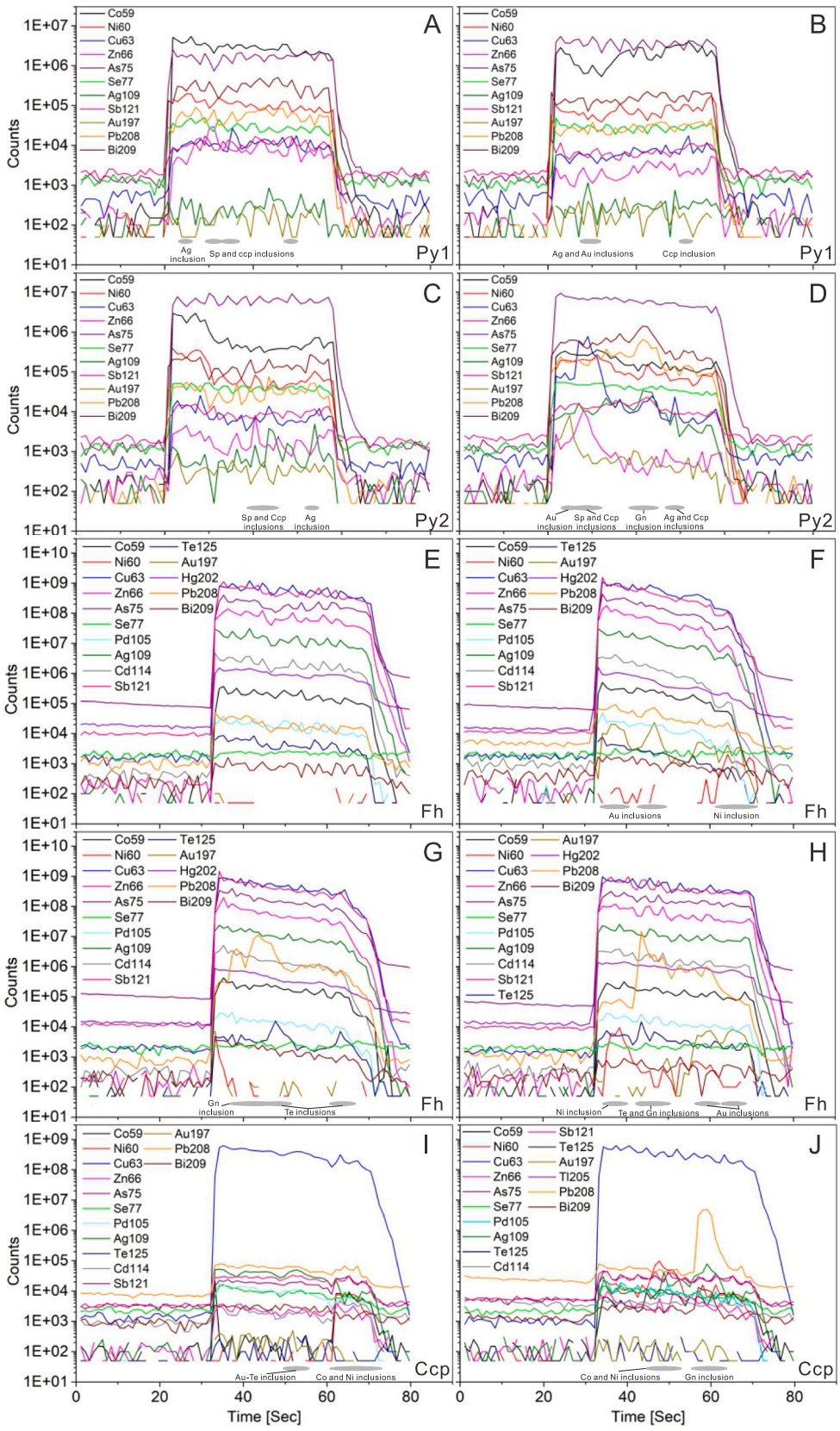

Fig. 7. Representative LA-ICP-MS spectra for selected elements in pyrites (A–D), fahlore (E–H) and chalcopyrite (I and J) from Kaldom Gol: (A) Smooth and parallel signals for Co, Ni, As and Se, and signals for Cu, Zn, Ag and Pb with numerous spikes; (B) The presence of several spikes in the signals for Cu, Zn, Ag, and Au indicates the occurrence of inclusions; (C) Spikes in the signals for Cu, Zn and Ag indicate the occurrence of inclusions in pyrite; (D) Spikes for Cu, Zn, Ag, Au, Pb and Bi imply the presence of inclusions; (E) Flat and parallel signals for all major and trace elements suggest their incorporation in fahlore's structure; (F) Spiky profiles by Au and Ni reflect native gold and Ni-inclusions; (G) Pb and Te spikes suggesting galena and telluride inclusions; (H) Rough signals for Ni, Te, Au, and Pb implying Ni-, telluride, native Au and galena inclusions, respectively; (I and J) Flat and parallel signals for Zn, As, Se, Pd, Ag, Cd and Sb indicate their incorporation in chalcopyrite's structure, while several rough signals for Co, Ni, Te, Au, Pb and Bi implying the presence of Co-Ni compounds, Au-tellurides inclusions and Ag-Bi bearing galena inclusions.

temperature chalcopyrite of the Cayeli deposit (62 ppm) NE Turkey (Revan et al., 2014).

In summary, based on Se contents in pyrite, the calculated crystallization temperature for Py1 and Py2 are 221–304 °C and 225–261 °C, respectively. Additionally, low Cd/Zn ratios in chalcopyrite suggest low to moderate temperatures (<400 °C) conditions. Moreover, our temperature estimates are consistent with the data from the fluid inclusion study by Tahirkheli et al. (1996), which indicate a temperature range of 160–350 °C.

5.3. Source of fluids inferred from sulfides

The relative amounts of As, Co, Ni, Au, Zn and Pb in pyrite have been successfully applied to determine the source of ore-forming fluid (Large et al., 2009; Yan et al., 2012). According to the binary plots and time-resolved depth profiles for various trace elements in pyrites from Kaldom Gol (this study; Section 5.1) that Au, Zn and Pb occur as mineral inclusions as well as in the crystal lattice of pyrite (e.g., Fig. 7A, C, D). Therefore, we have avoided using these elements for the genetic classification of pyrite. However, As, Co and Ni occur mostly within the pyrite crystal lattice.

The Co/Ni ratio can be used to classify the origin and source of fluids for pyrite mineralization (Bralia et al., 1979; Koglin et al., 2010; Zhang et al., 2014). A Co/Ni ratio of less than one indicates *syn*-sedimentary pyrite (Barbour, 1961; Clark et al., 2004), whereas a Co/Ni ratio of greater than one implies hydrothermal pyrite (e.g., Liu et al., 2018a; Adam et al., 2020). When determining the origin of pyrite, geological evidence such as mineralogical characteristics, the genetic type of ore deposit, and physicochemical characteristics of the ore-forming hydrothermal fluid (ligand concentration, redox, and temperature) as well as the relative partitioning of Co and Ni between co-crystallizing phases must be considered (Baidya et al., 2020). For example, at high salinity (up to 50 wt% NaCl) and temperatures (250–460 °C), Co shows more solubility and hence greater mobility than Ni. Similarly, the selective enrichment of Co over Ni in co-precipitated Co-pentlandite, cobaltian mackinawite and pyrrhotite may decrease the Co/Ni ratio. Compared to the high salinity levels (up to 50 wt% NaCl; Baidya et al., 2020), the polymetallic quartz veins at Kaldom Gol exhibit low (12.28–13.4 wt% $NaCl_{eq}$) and lack any Co and Ni-rich phases. Accordingly, pyrites (Py1 and Py2) from Kaldom Gol fall primarily within the field of hydrothermal pyrite (Co/Ni >1) and partly in the field of sedimentary pyrite (Co/Ni <1), which may have resulted from the mixing of the ore-forming fluid with crustal materials (Fig. 8A) (e.g., Liu et al., 2018b).

We use the As-Co-Ni diagram by Yan et al. (2012) to differentiate among pyrites from different geological environments, e.g., metamorphic, carlin-type and magmatic-hydrothermal. The elevated amounts of Co and As in pyrite, respectively, indicate the presence of magmatic water and meteoric water. When the volume of meteoric water exceeds that of the ore-forming fluid, the data points in the Co-Ni-As diagram tend to be closer to the As end. In contrast, the concentration of plotted data at the Co end suggests the predominance of magmatic water in the ore-forming fluid (e.g., Yan et al., 2012; Niu et al., 2016; Alam et al., 2019). The relative proportions of As-Co-Ni, implies that the Kaldom Gol pyrites (both Py1 and Py2) were formed by a magmatic-hydrothermal process (Fig. 8B). In the Co-Ni-As diagram, the plots are scattered between Co and As ends, but slightly closer to the As end than the Ni end (Fig. 8B), which may indicate the dominance of magmatic water and subsequent addition of meteoric water to the ore-forming fluids.

In general, homogeneous sulfur isotope compositions reflect a stable environment. Fluid-rock interactions (crustal contaminations), temperature changes, and mixing of the ore-forming fluid with meteoric water all contribute to the evolution of the S isotope compositions and, most likely, trace element contents of sulfides formed at different stages. For mixed-sulfide source deposits, the ^{34}S values range widely.

The sulfur isotopic composition of mantle-derived/magmatic fluids

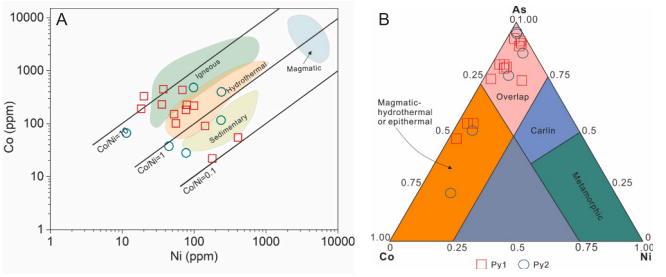

Fig. 8. Genetic characterization of pyrite mineralization at Kaldom Gol: (A) Most of the pyrite analyses have their Co/Ni ratios >1 (after Bajwah et al., 1987); (B) As-Co-Ni ternary plot indicating an exclusively magmatic-hydrothermal origin for the Kaldom Gol pyrite (after Brill, 1989; Yan et al., 2012; Niu et al., 2016; Yuan et al., 2018).

is generally close to 0 (±5 ‰) (Ohmoto, 1972; Chaussidon and Lorand, 1990). Hydrothermal fluids that form epithermal deposits can be primarily magmatic with high sulfidation (HS) or mainly meteoric with low sulfidation (LS) is noticed (Cooke and Simmons, 2000; Hedenquist et al., 2000). The range of $\delta^{34}S$ values (in ‰) for low, intermediate and high-sulfidation epithermal deposits are −6 to +5 (Ohmoto, 1979; Field and Fifarek, 1985), and −8 to +6 (Downes, 2007; Shahbazi et al., 2019; Madayag et al., 2021) and −10 to +8 ‰ (Arribas, 1995), respectively. The range of $\delta^{34}S$ (in ‰) for pyrite (Py1: $\delta^{34}S = -0.58$ to +2; and Py2: $\delta^{34}S = -0.24$ to +2.04) from Kaldom Gol (Fig. 9A) approximates the composition of sulfur isotopes from a single reservoir. Additionally, the sulfur isotope composition indicates that the ore fluids originated from a magmatic source with a low degree of crustal contamination, which makes the pyrite at Kaldom Gol comparable to the majority of epithermal deposits elsewhere in the world (Fig. 9B) (e.g., Christie and Robinson, 1992; Sabeva et al., 2017; Li et al., 2018; Liu et al., 2019; Shahbazi et al., 2019). On the basis of S-isotope data on pyrite, estimated age of the mineralization (~42 Ma) and spatial association with the Lowari intrusion (40–45 Ma), we suggest that the source of ore-forming fluids at Kaldom Gol was dominantly magmatic rather than metamorphic in origin.

Generally, magmatic-hydrothermal pyrite is characterized by low amounts of Bi (<1). However, the concentration of Bi could be high where the pyrite-forming magmatic-hydrothermal fluids interact with sedimentary rocks (Zierenberg et al., 1993; Keith et al., 2016). Previous research has demonstrated that sediment subduction influences the magmatic processes of the Brothers volcano (Haase et al., 2006; Timm et al., 2012) and Okinawa Trough (Shinjo, 1999). The transportation of Bi via magmatic volatiles from the magma chamber to the overlying hydrothermal systems of Brothers volcano (de Ronde et al., 2011; Berkenbosch et al., 2012) and Jade (Ishibashi et al., 2014) can most likely account for the higher Bi levels found in the respective pyrites. Consequently, fluid–sediment interaction or addition of a sedimentary component, e.g., through sediment subduction, to the magmatic-hydrothermal system may lead to higher Bi concentrations in the hydrothermal fluids and hence in the pyrite precipitating from them. Therefore, the elevated amount of Bi (>1 ppm) in pyrites (Py1 and Py2) from Kaldom Gol might have resulted from the addition of a sedimentary component to the hydrothermal system (Table 1).

5.4. Mineralization and ore genesis

The presence of the two pyrite types (Py1 and Py2) in Type I (a, b) mineral assemblages at Kaldom Gol suggests that they precipitated more or less contemporaneously from the evolving fluids. The replacement of Type I sulfides by fahlore and galena (Type II) suggests that the latter mineral assemblage was formed after Type I mineralization. Galena and fahlore from Type II show intergrown texture, indicating that both minerals formed simultaneously. Typically, the various types of

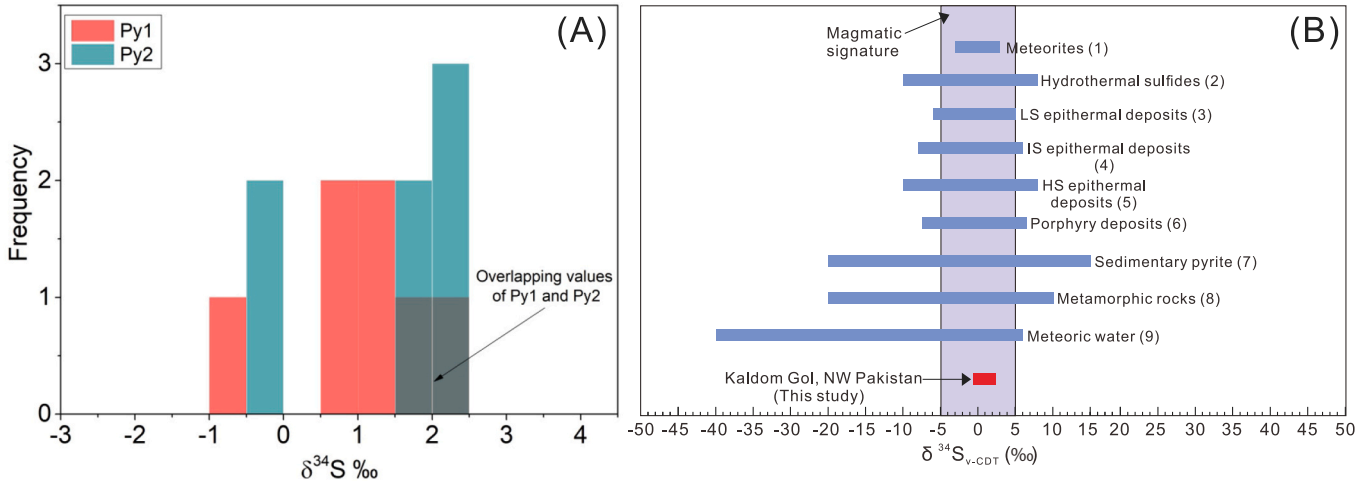

Fig. 9. (A) histogram showing in-situ sulfur isotope data on pyrite (Py1 and Py2) from Kaldom Gol; (B) comparison of the range of $\delta^{34}S$ values of the studied pyrite with sulfur isotopic compositions of different geological materials, Data sources: 1, Rollinson (1993); 2, Allegre (2008); 3, Ohmoto (1979) and Field and Fifarek (1985); 4, Downes (2007); 5, Arribas (1995); 6, Ohmoto (1979); 7, (Farquhar et al., 2010); 8, Hoefs (2004); 9, Barnes (1997).

epithermal deposits display distinct features and formations from fluids derived from different sources. In general, high-sulfidation (HS) epithermal deposits form from highly acidic fluids resulting from the interaction of acidic magmatic vapor with a smaller volume of groundwater (Arribas, 1995; Hedenquist et al., 1998). Low-sulfidation (LS) epithermal deposits are developed from fluids that are reduced, diluted and have close-to-neutral pH, resulting from the assimilation of magmatic components with deep-circulating groundwater (White and Hedenquist, 1995; Corbett and Leach, 1998; Corbett, 2002). Intermediate-sulfidation (IS) epithermal deposits show similar ore textures and alteration styles as LS epithermal deposits, but the fluids involved in IS mineralization are primarily magmatic with some groundwater component (Kouhestani et al., 2018; Mehrabi et al., 2019; Wang et al., 2019).

Most of the intermediate-sulfidation epithermal deposits are associated with calc-alkaline volcano-plutonic complexes in magmatic arcs (Sillitoe, 2010), and some occur in back-arc (e.g., öpler deposit; İmer et al., 2013), collisional, or post-subduction tectonic settings (e.g., Richards, 2009; Wang et al., 2019). Furthermore, most of the IS epithermal deposits are characterized by: 1) index epithermal textures (e.g., hydrothermal veins and breccias with vug infill, comb, banding, crustiform, and cockade textures); 2) hydrothermal alteration represented by quartz-adularia-illite-pyrite-sericite-carbonate; 3) relatively high abundance of base metals (e.g., Cu, Pb and Zn); 4) ore assemblage including chalcopyrite, Fe-poor sphalerite, galena, fahlore and other sulfosalts, 5) $\delta^{34}S$ composition of −10 ‰ to +8 ‰; 6) hydrothermal fluids temperature ranging between 155 and 330 ± 20 °C; 7) salinity ranging from <5 wt% to 24 wt% NaCleq., and 8) occurrence of shallow-level intrusive bodies adjacent to ore-bearing veins (e.g., Wang et al., 2019).

Mineralogy, texture (comb and bladed), sulfur isotope composition (Py1, −0.58 to +2; Py2, −0.24 to +2.04), estimated fluid temperature range (221–304 °C, Section 5.2) combined with fluid inclusion data from Tahirkheli et al. (1996) (Supplementary data S4; salinity from 12.28 to 13.40 wt% NaCl eq.) all group the Kaldom Gol deposit with typical IS epithermal deposits (Mehrabi et al., 2019; Wang et al., 2019). The geological and isotopic characteristics of the Kaldom Gol mineralization duplicate those of other epithermal mineral systems worldwide (Hedenquist et al., 2000; Simmons, 2005).

6. Conclusions

- Py1 and Py2 (pyrite) precipitation occurred at low to moderate temperatures, i.e., 221–304 °C and 225–261 °C, respectively.
- LA-ICP-MS time-resolved depth profiles confirm the presence of sulfosalt, sphalerite, and chalcopyrite inclusions in pyrite (Py1 and Py2) and of nickeliferous phases (e.g., *millerite*, *bravoite*, *vaesite*), Au-tellurides, native Au, and galena inclusions in chalcopyrite and fahlore.
- The Co/Ni (>1), Co-As-Ni diagram and the sulfur isotope composition (in ‰) of pyrite (Py1, −0.58 to +2; Py2, −0.24 to +2.04) from Kaldom Gol exhibits a typical magmatic-hydrothermal origin and is consistent with epithermal-type mineralization. The magmatic signatures of the ore suggest that the Lowari pluton (40–45 Ma) was responsible for the polymetallic mineralization (42 Ma) at Kaldom Gol.
- Gangue and sulfide minerals assemblages and their textures, in addition to sulfur isotope composition of pyrite and sulfide trace element contents, indicate that the mineralization is of intermediate sulfidation epithermal type.

Supplementary data to this article can be found online at https://doi.org/10.1016/j.chemer.2022.125949.

CRediT authorship contribution statement

Muhammad Farhan: Conceptualization, Methodology, Investigation, Writing – original draft, Visualization. **Mohammad Arif:** Writing – review & editing, Supervision. **Ying Ye:** Methodology, Validation, Supervision. **Chun-Feng Li:** Writing – review & editing, Project administration, Funding acquisition. **Xuegang Chen:** Resources. **Dieter Garbe-Schönberg:** Formal analysis. **Tao Wu:** Data curation. **Zaheen Ullah:** Investigation. **Zahid Hussain:** Investigation. **Tehseen Zafar:** Writing – review & editing. **Izhar Sadiq:** Resources. **Syed Wajid Hanif Bukhari:** Software. **Asad Khan:** Software.

Declaration of competing interest

The authors declare that they have no known competing financial interests or personal relationships that could have appeared to influence the work reported in this paper.

Acknowledgments

The authors would like to thank Ulrike Westernstroeer at Kiel University (Germany) for LA-ICP-MS analysis. We also thank the staff of the X-Ray Diffraction laboratory of Ocean College, Zhejiang University. The Chinese National Natural Science Foundation partially supported this study (Grant nos. 41761134051, 91858213, 41776057, 42176055). This research is also funded by Hainan Natural Science Foundation (Grant no. 21CXTD441). We gratefully acknowledge Prof. Dr. Astrid Holzheid, Dr. Abu Saeed Baidya, Dr. Verónica Bouhier and an anonymous reviewer for their constructive suggestions on the manuscript.

References

Abraitis, P., Pattrick, R., Vaughan, D., 2004. Variations in the compositional, textural and electrical properties of natural pyrite: a review. Int. J. Miner. Process. 74 (1–4), 41–59.

Adam, M.M., Lv, X., Rahman, A.A., Stern, R.J., Abdalrhman, A.A., Ullah, Z., 2020. In-situ sulfur isotope and trace element compositions of pyrite from the Neoproterozoic Haweit gold deposit, NE Sudan: implications for the origin and source of the sulfur. Ore Geol. Rev. 120, 103405.

Agheem, M., Shah, M., Khan, T., Ahmed, I., Laghari, A., Siddique, I., 2011. X-ray diffraction studies of gemstones from Shigar Valley, Skardu, Gilgit-Baltistan region, northern areas of Pakistan. Sindh Univ.Res.J. (Sci.Ser.) 43 (1).

Ai, M., Qin, W., Xia, T., Ye, Y., Chen, X., Zhang, P., 2019. Photocatalytic Degradation of 2,4-Dichlorophenol by TiO2 Intercalated Talc Nanocomposite. Int. J. Photoenergy 2019, 11.

Alam, M., Li, S.-R., Santosh, M., Shah, A., Yuan, M.-W., Khan, H., Qureshi, J.A., Zeng, Y.-J., 2019. Morphological, thermoelectrical, geochemical and isotopic anatomy of auriferous pyrite from the bagrote valley placer deposits, North Pakistan: implications for ore genesis and gold exploration. Ore Geol. Rev. 112, 103008.

Ali, L., Chapman, R., Farhan, M., Shah, M.T., Khattak, S.A., Ali, A., 2021. Exploration methodology using morphology and alloy composition of alluvial gold: a case study from quaternary deposits of the Nowshera District, Khyber Pakhtunkhwa, Pakistan. Min.Metall.Explor. 38 (1), 367–377.

Allegre, C.J., 2008. In: Isotope Geology. Cambridge University Press, pp. 358–428.

Anjum, M.N., Arif, M., Ali, L., 2018. Mineralogical and beneficiation studies of the Fe-Cu ores of Dammal Nisar, Chitral, NW Himalayas Pakistan. J.Himal.Earth Sci. 51 (2).

Arribas Jr., A., 1995. Characteristics of high-sulfidation epithermal deposits, and their relation to magmatic fluid. In: Mineralogical Association of Canada Short Course, 23, pp. 419–454.

Baidya, A.S., Sen, A., Pal, D.C., Upadhyay, D., 2020. Ore-forming processes in the Khetri Copper Belt, western India: constraints from trace element chemistry of pyrite and C-O isotope composition of carbonates. Mineral. Deposita 1–18.

Bajwah, Z.U., Seccombe, P.K., Offler, R., 1987. Trace element distribution Co:Ni ratios and genesis of the big cadia iron-copper deposit, New South Wales, Australia. Mineral. Deposita 22 (4).

Barbour, K.M., 1961. The Republic of the Sudan: A Regional Geography.

Barnes, H.L., 1997. Geochemistry of Hydrothermal Ore Deposits. John Wiley & Sons.

Berkenbosch, H., De Ronde, C., Gemmell, J., McNeill, A., Goemann, K., 2012. Mineralogy and formation of black smoker chimneys from brothers submarine volcano, Kermadec arc. Econ. Geol. 107 (8), 1613–1633.

Bignold, S., Treloar, P., 2003. Northward subduction of the Indian Plate beneath the Kohistan island arc, Pakistan Himalaya: new evidence from isotopic data. J. Geol. Soc. 160 (3), 377–384.

Bignold, S.M., Treloar, P.J., Petford, N., 2006. Changing sources of magma generation beneath intra-oceanic island arcs: an insight from the juvenile Kohistan island arc, Pakistan Himalaya. Chem. Geol. 233 (1–2), 46–74.

Bralia, A., Sabatini, G., Troja, F., 1979. A revaluation of the Co/Ni ratio in pyrite as geochemical tool in ore genesis problems. Mineral. Deposita 14 (3), 353–374.

Brill, B.A., 1989. Trace-element contents and partitioning of elements in ore minerals from the CSA Cu-Pb-Zn deposit, Australia, and implications for ore genesis. The Canadian Mineralogist 27 (2), 263–274.

Brindley, G., Brown, G., 1980. Crystal Structure of Clay Minerals and their X-ray Identification mineralogical Society, 143. Kaolinite Science, London, pp. 244–246.

Brown, G., Farrow, R., 1956. Introduction of glycerol into flake aggregates by vapour pressure. Clay Miner. Bull. 3 (15), 44–45.

Brunton, G., 1955. Vapor pressure glycolation of oriented clay minerals. Mineralogical Society of America.

Calkins, J.A., Jamiluddin, S., Bhuyan, K., Hussain, A., 1981. In: Geology And Mineral Resources of the Chitral-Partsan Area, Hindu Kush Range, Northern Pakistan. US Govt. Print. Off., pp. 2330–7102 for sale by the Distribution Branch, US Geological.

Chaussidon, M., Lorand, J.-P., 1990. Sulphur isotope composition of orogenic spinel lherzolite massifs from Ariege (North-Eastern Pyrenees, France): an ion microprobe study. Geochim. Cosmochim. Acta 54 (10), 2835–2846.

Christie, A.B., Robinson, B.W., 1992. Regional sulphur isotope studies of epithermal Au-Ag-Pb-Zn-Cu deposits in the Hauraki Goldfield, South Auckland. N. Z. J. Geol. Geophys. 35 (2), 145–150.

Clark, C., Grguric, B., Mumm, A.S., 2004. Genetic implications of pyrite chemistry from the Palaeoproterozoic Olary Domain and overlying Neoproterozoic Adelaidean sequences, northeastern South Australia. Ore Geol. Rev. 25 (3–4), 237–257.

Cooke, D.R., Simmons, S.F., 2000. Characteristics And Genesis of Epithermal Gold Deposits.

Corbett, G., 2002. Epithermal gold for explorationists: AIG Presidents Lecture. AIG Online J. April. 67, 1–8.

Corbett, G.J., Leach, T.M., 1998. Southwest Pacific Rim Gold-copper Systems: Structure, Alteration, And Mineralization. Society of Economic Geologists Boulder Co.

Coward, M.P., Rex, D.C., Khan, M.A., Windley, B.F., Broughton, R.D., Luff, I.W., Petterson, M.G., Pudsey, C.J., 1986. Collision tectonics in the NW Himalayas. Geol. Soc. Lond. Spec. Publ. 19 (1), 203–219.

de Ronde, C.E., Massoth, G.J., Butterfield, D.A., Christenson, B.W., Ishibashi, J., Ditchburn, R.G., Hannington, M.D., Brathwaite, R.L., Lupton, J.E., Kamenetsky, V.S., 2011. Submarine hydrothermal activity and gold-rich mineralization at Brothers Volcano, Kermadec Arc,New Zealand. Mineral. Deposita 46 (5), 541–584.

Deditius, A.P., Reich, M., Kesler, S.E., Utsunomiya, S., Chryssoulis, S.L., Walshe, J., Ewing, R.C., 2014. The coupled geochemistry of Au and As in pyrite from hydrothermal ore deposits. Geochim. Cosmochim. Acta 140, 644–670.

Downes, P.M., 2007. Yerranderie a Late Devonian silver–gold–lead intermediate sulfidation epithermal district, eastern Lachlan orogen, New South Wales, Australia. Resour. Geol. 57 (1), 1–23.

Farhan, M., Arif, M., Ying, Y., Chen, X., Garbe-Schönberg, D., Li, C.-F., Hussain, Z., Ullah, Z., Zhang, P., Khan, A., 2021a. Fluid source, element mobility and physicochemical conditions of porphyry-style hydrothermal alteration-mineralization at Mirkhani, southern Chitral, Pakistan. Ore Geol. Rev. 135, 1–32, 104222.

Farhan, M., Arif, M., Ying, Y., Chen, X., Garbe-Schönberg, D., Ullah, Z., Sadiq, I., 2021b. Host rock peculiarities and influence of major structures on gold and base metal sulfide mineralization in northern Pakistan. Period.Mineral. 90 (1), 137–171.

Farquhar, J., Wu, N., Canfield, D.E., Oduro, H., 2010. Connections between sulfur cycle evolution, sulfur isotopes, sediments, and base metal sulfide deposits. Econ. Geol. 105 (3), 509–533.

Field, C.W., Fifarek, R.H., 1985. Light Stable-isotope Systematics in the Epithermal Environment.

Fonseca, R.M., Barriga, F.J., Conceição, P.I., 2010. Clay minerals in sediments of Portuguese reservoirs and their significance as weathering products from over-eroded soils: a comparative study of the Maranhão, Monte Novo and Divor Reservoirs (South Portugal). Int. J. Earth Sci. 99, 1899–1916.

George, L.L., 2017. Trace element distributions and partitioning trends in hydrothermal base metal sulphide ores comprising sphalerite, galena, chalcopyrite and tetrahedrite-tennantite.

George, L.L., Cook, N.J., Ciobanu, C.L., 2017. Minor and trace elements in natural tetrahedrite-tennantite: effects on element partitioning among base metal sulphides. Minerals 7 (2), 17.

George, L.L., Cook, N.J., Crowe, B.B., Ciobanu, C.L., 2018. Trace elements in hydrothermal chalcopyrite. Mineral. Mag. 82 (1), 59–88.

Giri, R.K., Pandit, D., Rao, C., 2018. Cobaltoan pyrite in a lamprophyre from the Sidhi Gneissic Complex, Mahakoshal Belt, Central India. J. Geol. Soc. India 91, 5–8.

González-Álvarez, I., Pirajno, F., Kerrich, R., 2013. In: Hydrothermal Nickel Deposits: Secular Variation And Diversity. Elsevier, pp. 1–3.

Haase, K.M., Stroncik, N., Garbe-Schönberg, D., Stoffers, P., 2006. Formation of island arc dacite magmas by extreme crystal fractionation: an example from Brothers Seamount, Kermadec island arc (SW Pacific). J. Volcanol. Geotherm. Res. 152 (3–4), 316–330.

Hedenquist, J.W., Arribas, A., Gonzalez-Urien, E., 2000. Exploration for epithermal gold deposits. Rev. Econ. Geol. 13 (2), 45–77.

Hedenquist, J.W., Arribas, A., Reynolds, T.J., 1998. Evolution of an intrusion-centered hydrothermal system; Far Southeast-Lepanto porphyry and epithermal Cu-Au deposits,Philippines. Econ. Geol. 93 (4), 373–404.

Herrington, R., Brown, D., 2011. The Generation And Preservation of Mineral Deposits in Arc–Continent Collision Environments for sale by the Distribution Branch, US Geological.

Hoefs, J., 2004. Isotope fractionation mechanisms of selected elements. In: Stable Isotope Geochemistry. Springer, pp. 31–76.

Hussain, Z., Tao, C., Li, C.-F., Liao, S., Alam, M., Farhan, M., Zhang, H., Hussain, A., 2021. Mineralogy, fluid inclusions, and isotopic study of the Kargah Cu-Pb polymetallic vein-type deposit, Kohistan Island arc, northern Pakistan: implication for ore genesis. Minerals 11 (11), 1266.

Huston, D.L., Sie, S.H., Suter, G.F., Cooke, D.R., Both, R.A., 1995. Trace elements in sulfide minerals from eastern Australian volcanic-hosted massive sulfide deposits; part I, proton microprobe analyses of pyrite, chalcopyrite, and sphalerite, and part II, selenium levels in pyrite; comparison with delta 34 S values and implications for the source of sulfur in volcanogenic hydrothermal systems. Econ. Geol. 90 (5), 1167–1196.

İmer, A., Richards, J.P., Creaser, R.A., 2013. Age and tectonomagmatic setting of the Eocene Çöpler-Kabataş magmatic complex and porphyry-epithermal Au deposit, East Central Anatolia,Turkey. Mineral. Deposita 48 (5), 557–583.

Ishibashi, J.-I., Noguchi, T., Toki, T., Miyabe, S., Yamagami, S., Onishi, Y., Yamanaka, T., Yokoyama, Y., Omori, E., Takahashi, Y., 2014. Diversity of fluid geochemistry affected by processes during fluid upwelling in active hydrothermal fields in the Izena Hole, the middle Okinawa Trough back-arc basin. Geochem. J. 48 (4), 357–369.

Ishida, M., Romero, R., Leisen, M., Yasukawa, K., Nakamura, K., Barra, F., Reich, M., Kato, Y., 2022. Auriferous pyrite formed by episodic fluid inputs in the Akeshi and Kasuga high-sulfidation deposits, Southern Kyushu,Japan. Mineral. Deposita 57 (1), 129–145.

Keith, M., Häckel, F., Haase, K.M., Schwarz-Schampera, U., Klemd, R., 2016. Trace element systematics of pyrite from submarine hydrothermal vents. Ore Geol. Rev. 72, 728–745.
Keith, M., Smith, D.J., Jenkin, G.R., Holwell, D.A., Dye, M.D., 2018. A review of Te and Se systematics in hydrothermal pyrite from precious metal deposits: insights into ore-forming processes. Ore Geol. Rev. 96, 269–282.
Khan, M.A., Stern, R.J., Gribble, R.F., Windley, B.F., 1997. Geochemical and isotopic constraints on subduction polarity, magma sources, and palaeogeography of the Kohistan intra-oceanic arc, northern Pakistan Himalaya. J. Geol. Soc. 154 (6), 935–946.
Koglin, N., Frimmel, H.E., Minter, W.L., Brätz, H., 2010. Trace-element characteristics of different pyrite types in Mesoarchaean to Palaeoproterozoic placer deposits. Mineral. Deposita 45 (3), 259–280.
Kouhestani, H., Mokhtari, M.A.A., Chang, Z., Johnson, C.A., 2018. Intermediate sulfidation type base metal mineralization at Aliabad-Khanchy, Tarom-Hashtjin metallogenic belt, NW Iran. Ore Geol. Rev. 93, 1–18.
Large, R.R., Danyushevsky, L., Hollit, C., Maslennikov, V., Meffre, S., Gilbert, S., Bull, S., Scott, R., Emsbo, P., Thomas, H., 2009. Gold and trace element zonation in pyrite using a laser imaging technique: implications for the timing of gold in orogenic and Carlin-style sediment-hosted deposits. Econ. Geol. 104 (5), 635–668.
Li, S.-N., Ni, P., Bao, T., Xiang, H.-L., Chi, Z., Wang, G.-G., Huang, B., Ding, J.-Y., Dai, B.-Z., 2018. Genesis of the Ancun epithermal gold deposit, southeast China: evidence from fluid inclusion and stable isotope data. J. Geochem. Explor. 195, 157–177.
Li, Z.-K., Li, J.-W., Cooke, D.R., Danyushevsky, L., Zhang, L., O'Brien, H., Lahaye, Y., Zhang, W., Xu, H.-J., 2016. Textures, trace elements, and Pb isotopes of sulfides from the Haopinggou vein deposit, southern North China Craton: implications for discrete au and Ag–Pb–Zn mineralization. Contrib. Mineral. Petrol. 171 (12), 1–26.
Liu, Y., Sun, J., Han, J., Ren, L., Gu, A., Zhao, K., Wang, C., 2019. Origin and evolution of ore-forming fluid for the Gaosongshan gold deposit, Lesser Xing'an Range: Evidence from fluid inclusions, H-O-S-Pb isotopes. Geosci. Front. 10 (5), 1961–1980.
Liu, Z., Mao, X., Deng, H., Li, B., Zhang, S., Lai, J., Bayless, R.C., Pan, M., Li, L., Shang, Q., 2018a. Hydrothermal processes at the Axi epithermal Au deposit, western tianshan: insights from geochemical effects of alteration, mineralization and trace elements in pyrite. Ore Geol. Rev. 102, 368–385.
Liu, Z., Shao, Y., Zhou, H., Liu, N., Huang, K., Liu, Q., Zhang, J., Wang, C., 2018b. Major and trace element geochemistry of pyrite and pyrrhotite from stratiform and lamellar orebodies: implications for the ore genesis of the Dongguashan copper (gold) deposit,eastern China. Minerals 8 (9), 380.
Mackenzie, R., Farquharson, K., 1956. A method for concentration of dilute clay suspensions without coagulation. Clay Miner. Bull. 3 (15), 7.
Madayag, E., Graham, I., Quan, H., Worland, R., Adler, L., Dietz, C., 2021. Mineralization, alteration assemblages and stable isotopes of the intermediate-sulfidation epithermal Strauss deposit, Drake Goldfield, north-eastern NSW, Australia. In: Environmental Sciences Proceedings. Multidisciplinary Digital Publishing Institute, p. 27.
Maslennikov, V., Maslennikova, S., Large, R., Danyushevsky, L., 2009. Study of trace element zonation in vent chimneys from the Silurian Yaman-Kasy volcanic-hosted massive sulfide deposit (Southern Urals, Russia) using laser ablation-inductively coupled plasma mass spectrometry (LA-ICPMS). Econ. Geol. 104 (8), 1111–1141.
Mehrabi, B., Tale Fazel, E., Yardley, B., 2019. Ore geology, fluid inclusions and O-S stable isotope characteristics of Shurab Sb-polymetallic vein deposit, eastern Iran. Geochemistry 79 (2), 307–322.
Mitchell, A.H., Bell, J.D., 1973. Island-arc evolution and related mineral deposits. J.Geol. 81, 381–405.
Morishita, Y., Hammond, N.Q., Momii, K., Konagaya, R., Sano, Y., Takahata, N., Ueno, H., 2019. Invisible gold in pyrite from epithermal, banded-iron-formation-hosted, and sedimentary gold deposits: evidence of hydrothermal influence. Minerals 9 (7), 447.
Mosser-Ruck, R., Devineau, K., Charpentier, D., Cathelineau, M., 2005. Effects of ethylene glycol saturation protocols on XRD patterns: a critical review and discussion. Clay Clay Miner. 53, 631–638.
Niu, S.-D., Li, S.-R., Santosh, M., Zhang, D.-H., Li, Z.-D., Shan, M.-J., Lan, Y.-X., Gao, D.-R., Zhao, W.-B., 2016. Mineralogical and isotopic studies of base metal sulfides from the Jiawula Ag–Pb–Zn deposit, Inner Mongolia, NE China. J. Asian Earth Sci. 115, 480–491.
Ohmoto, H., 1972. Systematics of sulfur and carbon isotopes in hydrothermal ore deposits. Econ. Geol. 67 (5), 551–578.
Ohmoto, H., 1979. Isotopes of sulfur and carbon. In: Geochemistry of Hydrothermal Ore Deposits, pp. 509–567.
Petterson, M.G., 2010. A review of the geology and tectonics of the Kohistan island arc, north Pakistan. Geol. Soc. Lond. Spec. Publ. 338 (1), 287–327.
Pudsey, C., Coward, M., Luff, I., Shackleton, R., Windley, B., Jan, M., 1985. Collision zone between the Kohistan arc and the Asian plate in NW Pakistan. Earth Environ. Sci. Trans. R. Soc. Edinb. 76 (4), 463–479.
Ramachandran, V.S., Beaudoin, J.J., 2000. Handbook of analytical techniques in concrete science and technology: principles, techniques and applications. Elsevier.
Reich, M., Kesler, S.E., Utsunomiya, S., Palenik, C.S., Chryssoulis, S.L., Ewing, R.C., 2005. Solubility of gold in arsenian pyrite. Geochim. Cosmochim. Acta 69 (11), 2781–2796.
Repstock, A., Voudouris, P., Zeug, M., Melfos, V., Zhai, M., Li, H., Kartal, T., Matuszczak, J., 2016. Chemical composition and varieties of fahlore-group minerals from Oligocene mineralization in the Rhodope area, Southern Bulgaria and Northern Greece. Mineral. Petrol. 110 (1), 103–123.
Revan, M.K., Genç, Y., Maslennikov, V.V., Maslennikova, S.P., Large, R.R., Danyushevsky, L.V., 2014. Mineralogy and trace-element geochemistry of sulfide minerals in hydrothermal chimneys from the Upper-Cretaceous VMS deposits of the eastern Pontide orogenic belt (NE Turkey). Ore Geol. Rev. 63, 129–149.
Richards, J.P., 2009. Postsubduction porphyry Cu-Au and epithermal Au deposits: products of remelting of subduction-modified lithosphere. Geology 37 (3), 247–250.
Rollinson, H., 1993. Using geochemical data. In: Evaluation, Presentation, Interpretation, 1.
Sabeva, R., Mladenova, V., Mogessie, A., 2017. Ore petrology, hydrothermal alteration, fluid inclusions, and sulfur stable isotopes of the Milin Kamak intermediate sulfidation epithermal Au-Ag deposit in Western Srednogorie, Bulgaria. Ore Geol. Rev. 88, 400–415.
Sack, R.O., 2005. Internally consistent database for sulfides and sulfosalts in the system Ag2S-Cu2S-ZnS-FeS-Sb2S3-As2S3: update. Geochim. Cosmochim. Acta 69 (5), 1157–1164.
Sack, R.O., Lichtner, P.C., 2009. Constraining compositions of hydrothermal fluids in equilibrium with polymetallic ore-forming sulfide assemblages. Econ. Geol. 104 (8), 1249–1264.
Searle, M., Khan, M.A., Fraser, J., Gough, S., Jan, M.Q., 1999. The tectonic evolution of the Kohistan-Karakoram collision belt along the Karakoram Highway transect, North Pakistan. Tectonics 18 (6), 929–949.
Shahbazi, S., Ghaderi, M., Alfonso, P., 2019. Mineralogy, alteration, and sulfur isotope geochemistry of the Zehabad intermediatesulfidation epithermal deposit, NW Iran. Turk. J. Earth Sci. 28 (6), 882–901.
Shao, Y.-J., Wang, W.-S., Liu, Q.-Q., Zhang, Y., 2018. Trace element analysis of pyrite from the Zhengchong gold deposit, Northeast Hunan Province, China: implications for the ore-forming process. Minerals 8 (6), 262.
Shinjo, R., 1999. Geochemistry of high Mg andesites and the tectonic evolution of the Okinawa Trough-Ryukyu arc system. Chem. Geol. 157 (1–2), 69–88.
Sillitoe, R.H., 2010. Porphyry copper systems. Econ. Geol. 105 (1), 3–41.
Simmons, S.F., 2005. In: Geological Characteristics of Epithermal Precious And Base Metal Deposits, 100th anniversary volume, pp. 485–522.
Tahirkheli, T., Khan, M.A., Shah, M.T., 2005. Geochemistry and petrogenesis of metavolcanic rocks in Gawuch and Drosh formations, Chitral, northern Pakistan. Geol.Bull.Univ.Peshawar 38, 189–202.
Tahirkheli, T., Shah, M.T., Khan, M.A., 1997. Lead isotopic signature of the hydrothermal copper mineralization in Droshi-Shishi Area, Chitral, Kohistan Arc Terrane, Northern Pakistan. Geol.Bull.Univ.Peshawar 30, 209–217.
Tahirkheli, T., Shah, M.T., Khan, M.A., Bilqees, R., 2012. Mineralogy and geochemistry of diorites and associated hydrothermal sulfide mineralization of Gawuch Formation in Drosh area, Chitral, northern Pakistan. J.Himal.Earth Sci. 45 (1).
Tahirkheli, T., Shah, M.T., Khan, T., Khan, M.A., 1996. Fluid inclusion studies of the copper-bearing quartz veins in Gowuch Formation, Drosh-Shishi area, Chitral, northern Pakistan. Geol.Bull.Univ.Peshawar 29, 51–57.
Timm, C., de Ronde, C.E., Leybourne, M.I., Layton-Matthews, D., Graham, I.J., 2012. Sources of chalcophile and siderophile elements in Kermadec arc lavas. Econ. Geol. 107 (8), 1527–1538.
Ullah, Z., Khan, A., Faisal, S., Zafar, T., Li, H., Farhan, M., 2022a. Petrogenesis of peridotites in the Dargai Complex ophiolite, Indus Suture Zone, Northern Pakistan: implications for two stages of melting, depletion, and enrichment of the Neo-Tethyan mantle. Lithos 426, 106798.
Ullah, Z., Li, H., Khan, A., Faisal, S., Dilek, Y., Förster, M.W., Farhan, M., Ashraf, U., Khattak, S.A., Rehman, G., 2022b. Mineralogy and PGE geochemistry of chromitites and peridotites of the sapat complex in the indus suture zone, northern Pakistan: implications for magmatic processes in the supra-subduction zone. Int. Geol. Rev. 1–26.
Wang, L., Qin, K.-Z., Song, G.-X., Li, G.-M., 2019. A review of intermediate sulfidation epithermal deposits and subclassification. Ore Geol. Rev. 107, 434–456.
Wei, D., Xia, Y., Steadman, J.A., Xie, Z., Liu, X., Tan, Q., Bai, L.a., 2020. Tennantite–tetrahedrite-series minerals and related pyrite in the Nibao Carlin-type gold deposit, Guizhou, SW China. Minerals 11 (1), 2.
White, N.C., Hedenquist, J.W., 1995. Epithermal gold deposits: styles, characteristics and exploration. SEG Newsl. 23 (1), 9–13.
Xu, S., 2005. Mineralogy characteristic and the genetic significance of tennantite-tetrahedrite from Ag-Cu-Co-Ni polymetal deposits in Lanping basin, Yunnan,China. J. Chengdu Univ. Technol. 32 (6), 556.
Yan, Y.T., Li, S.R., Jia, B.J., Zhang, N., Jiang, L., Yan, L.N., 2012. Composition typomorphic characteristics of pyrite in various genetic type gold deposits. In: Advanced Materials Research. Trans Tech Publ, pp. 25–29.
Yuan, M.-W., Li, S.-R., Li, C.-L., Santosh, M., Alam, M., Zeng, Y.-J., 2018. Geochemical and isotopic composition of auriferous pyrite from the Yongxin gold deposit, Central Asian Orogenic Belt: implication for ore genesis. Ore Geol. Rev. 93, 255–267.
Zaman, H., Bamousa, A.O., 2015. Magnetomineralogical changes along the Kohistan-Karakoram collision zone inNorth Pakistan: implications for variable thermochemical activities. Turk. J. Earth Sci. 24, 179–195.
Zanchi, A., Gaetani, M., 2011. The geology of the Karakoram range, Pakistan: the new 1: 100,000 geological map of Central-Western Karakoram. Ital. J. Geosci. 130 (2), 161–262.
Zeitler, P.K., 1985. Cooling history of the NW Himalaya,Pakistan. Tectonics 4 (1), 127–151.
Zhang, H., Ling, M.-X., Liu, Y.-L., Tu, X.-L., Wang, F.-Y., Li, C.-Y., Liang, H.-Y., Yang, X.-Y., Arndt, N.T., Sun, W.-D., 2013. High oxygen fugacity and slab melting linked to Cu mineralization: evidence from Dexing porphyry copper deposits, southeastern China. J.Geol. 121 (3), 289–305.
Zhang, J., Deng, J., Chen, H.-Y., Yang, L.-Q., Cooke, D., Danyushevsky, L., Gong, Q.-J., 2014. LA-ICP-MS trace element analysis of pyrite from the Chang'an gold deposit,

Sanjiang region, China: implication for ore-forming process. Gondwana Res. 26 (2), 557–575.
Zhou, C., Yang, Z., Sun, H., Koua, K.A.D., Lyu, C., 2022. LA-ICP-MS trace element analysis of sphalerite and pyrite from the Beishan Pb-Zn ore district, South China: implications for ore genesis. Ore Geol. Rev. 150, 14, 105128.
Zierenberg, R.A., Koski, R.A., Morton, J.L., Bouse, R.M., 1993. Genesis of massive sulfide deposits on a sediment-covered spreading center, Escanaba Trough, southern Gorda Ridge. Econ. Geol. 88 (8), 2069–2098.

Further reading

Seal, R.R., 2006. Sulfur isotope geochemistry of sulfide minerals. Rev. Mineral. Geochem. 61 (1), 633–677.